Draft version January 1, 2022
Typeset using LaTeX **twocolumn** style in AASTeX63

arXiv:2009.07729v1 [astro-ph.EP] 16 Sep 2020

ALMA Observations of Io Going into and Coming out of Eclipse

Imke de Pater,[1] Statia Luszcz-Cook,[2] Patricio Rojo,[3] Erin Redwing,[4] Katherine de Kleer,[5] and Arielle Moullet[6]

[1] *University of California, 501 Campbell Hall, Berkeley, CA 94720, USA, and Faculty of Aerospace Engineering, Delft University of Technology, Delft 2629 HS, The Netherlands*
[2] *University of Columbia, Astronomy Department, New York, USA*
[3] *Universidad de Chile, Departamento de Astronomia, Casilla 36-D, Santiago, Chile*
[4] *University of California, 307 McCone Hall, Berkeley, CA 94720, USA*
[5] *California Institute of Technology, 1200 East California Boulevard, Pasadena, CA 91101, USA*
[6] *SOFIA/USRA, NASA Ames Building N232, Moffett Field, CA 94035, USA*

(Received XXX; Revised XXX; Accepted XXX)

Submitted to Planetary Science Journal

ABSTRACT

We present 1-mm observations constructed from ALMA [Atacama Large (sub)Millimeter Array] data of SO_2, SO and KCl when Io went from sunlight into eclipse (20 March 2018), and vice versa (2 and 11 September 2018). There is clear evidence of volcanic plumes on 20 March and 2 September. The plumes distort the line profiles, causing high-velocity ($\gtrsim$500 m/s) wings, and red/blue-shifted shoulders in the line profiles. During eclipse ingress, the SO_2 flux density dropped exponentially, and the atmosphere reformed in a linear fashion when re-emerging in sunlight, with a "post-eclipse brightening" after $\sim$10 minutes. While both the in-eclipse decrease and in-sunlight increase in SO was more gradual than for SO_2, the fact that SO decreased at all is evidence that self-reactions at the surface are important and fast, and that in-sunlight photolysis of SO_2 is the dominant source of SO. Disk-integrated SO_2 in-sunlight flux densities are $\sim$2–3 times higher than in-eclipse, indicative of a roughly 30–50% contribution from volcanic sources to the atmosphere. Typical column densities and temperatures are $N \approx (1.5 \pm 0.3) \times 10^{16}$ cm^{-2} and $T \approx 220 - 320$ K both in-sunlight and in-eclipse, while the fractional coverage of the gas is 2–3 times lower in-eclipse than in-sunlight. The low level SO_2 emissions present during eclipse may be sourced by stealth volcanism or be evidence of a layer of non-condensible gases preventing complete collapse of the SO_2 atmosphere. The melt in magma chambers at different volcanoes must differ in composition to explain the absence of SO and SO_2, but simultaneous presence of KCl over Ulgen Patera.

Keywords: Galilean satellites, Planetary atmospheres, Radio astronomy

1. INTRODUCTION

Jupiter's satellite Io is unique amongst bodies in our Solar System. Its yellow-white-orange-red coloration is produced by SO_2-frost on its surface, a variety of sulfur allotropes (S_2–S_{20}), and metastable polymorphs of elemental sulfur mixed in with other species (Moses and Nash, 1991). Spectra of the numerous dark calderas, sites of intermittant volcanic activity, indicate the presence of (ultra)mafic minerals such as olivine and pyroxene (Geissler et al., 1999). When Io is in eclipse (Jupiter's shadow), or during an ionian night (visible only from spacecraft), visible and near-infrared images of the satellite reveal dozens of thermally-bright volcanic hot spots (e.g., Geissler et al., 2001; Macintosh et al., 2003; de Pater et al, 2004; Spencer et al., 2007; Retherford et al., 2007). This widespread volcanic activity is powered by strong tidal heating induced by Io's orbital eccentricity, which is the result of the Laplace orbital resonance between Io, Europa, and Ganymede. Some volcanoes are associated with active plumes, which are a major source of material into Io's atmosphere, Jupiter's magnetosphere, and even the interplanetary medium. The mass-loss from Io's atmosphere is estimated at 1 ton/second (Spencer and Schneider, 1996), yet the atmosphere is consistently present, indicating an ongoing replenishment mechanism. However, the amount of ma-

terial pumped into Io's atmosphere by volcanism is not well known, and it is consequently not known whether the dynamics in Io's atmosphere is primarily driven by sublimation of SO_2 frost on its surface or by volcanoes. An additional source of atmospheric gas may be sputtering from Io's surface.

A decade after the inital detection of gaseous SO_2 in its ν_3 band (7.3 μm) from the Voyager data (Pearl et al., 1979), Io's "global" SO_2 atmosphere was detected at 222 GHz (Lellouch et al., 1990). These data revealed a surface pressure of order 4–40 nbars (2×10^{17}–2×10^{18} cm^{-2}), covering 3–20% of the surface, at temperatures of $\sim$ 500-600 K. There is a large uncertainty in the temperature, however, since it is extremely difficult to disentangle the contributions of density, temperature and fractional coverage[1] in the line profiles (e.g., Lellouch et al., 1992). Moreover, zonal winds would broaden the line profile ("competing" with temperature), while Ballester et al (1994) noted that winds from volcanic eruptions may distort the lineshape, both adding complications to modeling efforts. Although SO_2 has now been observed at mm, UV, and at thermal infrared wavelengths, its temperature and column density are still poorly constrained.

Based upon photochemical considerations alone, in a SO_2-dominated atmosphere one would expect at least the products SO, O_2, as well as atomic S and O (e.g., Kumar, 1985; Summers, 1985). SO was detected at microwave wavelengths at a level of a few % compared to the SO_2 abundance (Lellouch, 1996). While O_2 has not (yet) been detected, S and O have been detected e.g., in the form of auroral emissions off Io's limb along its equator (e.g., Geissler et al. 2004). We further note that gaseous NaCl was first detected by Lellouch et al. (2003), and a tentative detection of KCl was reported by Moullet et al. (2013). Both NaCl and KCl were mapped with ALMA by Moullet et al. (2015).

Spatially resolved data obtained with the Hubble Space Telescope (HST) at UV wavelengths revealed that SO_2 was mainly confined to latitudes within 30–40° from the equator, with a higher column density and latitudinal extent on the anti-jovian side (central meridian longitude CML $\sim$180°W) (e.g., Roesler et al., 1999; Feaga et al., 2004, 2009). The sub- (CML $\sim$0°W) to anti-jovian hemisphere distribution was confirmed using disk-averaged thermal infrared data of the 19-μm ν_2 band of SO_2, observed in absorption against Io with the TEXES instrument on NASA's Infrared Telescope Facility (IRTF) in 2001–2005 (Spencer et al., 2005). While these observations showed a temperature of $\sim$115-120 K, interpretation of disk-resolved observations of the SO_2 $\nu_1+\nu_3$ band at 4 μm with the CRIRES instrument on the Very Large Telescope (VLT) favors a temperature of $\sim$170 K (Lellouch et al., 2015). Typical column densities in all these data vary roughly from $\sim 10^{16}$ on the sub-jovian hemisphere to $\sim 10^{17}$ cm^{-2} on the anti-jovian side.

Moullet et al. (2010) used the spatial distribution derived from the HST/UV and TEXES/IRTF observations to analyze SO_2 maps at mm-wavelengths obtained with the Sub-Millimeter Array (SMA). By decreasing the number of free parameters to just temperature and column density, using the fractional coverage from the UV and mid-IR data, they derived a disk-averaged column density of 2.3–4.6$\times10^{16}$ cm^{-2} and temperature between 150–210 K on the leading (CML $\sim$ 90°W) hemisphere, and 0.7–1.1$\times10^{16}$ cm^{-2} with 215–255 K on the trailing (CML $\sim$ 270°W) side. These temperatures and column densities are considerably lower than the earlier mm-wavelength measurements.

As mentioned above, it is still being debated whether the primary source of Io's atmosphere is volcanic or driven by sublimation, although it is clear that both volcanoes and SO_2 frost do play a role (Jessup et al., 2007; Lellouch et al., 1990, 2003, 2015; Moullet et al., 2010, 2013, 2015; Spencer et al., 2005; Tsang et al., 2012, 2016). Although much of the SO_2 frost may ultimately have been produced by volcanoes, the extent to which volcanoes directly affect the atmosphere is unknown; moreover, this likely varies over time. Mid-IR observations showed an increase in the SO_2 abundance with decreasing heliocentric distance, which is, at least in part, in support of the sublimation theory (Tsang et al., 2012). Further support was given by the analysis of the SMA maps mentioned above, which indicated that frost sublimation is the main source of gaseous SO_2, and photolysis of SO_2 is the main source of SO, since volcanic activity is not sufficient to explain the SO column density and distribution (Moullet et al., 2010). On the other hand, SO_2 gas is enhanced above some volcanic hot spots (McGrath et al., 2000) , and Pele's plume contains the sulfur-rich gases S_2, S, and SO (McGrath et al., 2000, Spencer et al., 2000; Jessup et al., 2007), indicative of volcanic contributions to Io's atmosphere. For more information on the pros and cons of the driving forces (sublimation vs volcanic) of Io's atmospheric dynamics, see the excellent reviews of the state-of-knowledge of Io's atmosphere in the mid-2000's by McGrath et al. (2004) and Lellouch et al. (2007).

[1] The fractional coverage of the gas is the fraction of the projected surface that is covered by the gas.

Observations of Io right before, after and during an eclipse provide the best way to separate the volcanic from sublimation-driven contributions to its atmosphere. The atmospheric temperature is expected to drop within minutes after Io enters an eclipse (e.g., de Pater et al., 2002). The SO_2 gas that makes up the bulk of Io's atmosphere is expected to condense out on a similar timescale, set by the vapor pressure of this gas, which is a steep exponential function of temperature ($P_{vapor} = 1.52 \times 10^8 e^{-4510/T}$ bar; Wagman, 1979).

Tsang et al (2016) obtained the first direct obervations of the SO_2 ν_2 band in Io's atmosphere in eclipse with the TEXES instrument on the Gemini telescope. Their disk-integrated spectra were sensitive to surface temperature, atmospheric temperature, and SO_2 column abundance. Based on a simple model with a surface temperature of 127 K, they found that this value dropped to 105 K within minutes after entering eclipse. A range of models for Io's atmospheric cooling all showed that the SO_2 column density simultaneously dropped, by a factor of 5±2. They therefore concluded that the atmosphere must contain a large component that is driven by sublimation.

Although the radical SO will not condense at these temperatures, it may be rapidly removed from the atmosphere through reactions with Io's surface (Lellouch et al. 1996). However, a bright emission band complex at 1.707 μm, the forbidden electronic $a^1\Delta \rightarrow X^3\Sigma^-$ transition of SO, was observed in a disk-integrated spectrum of Io while in eclipse. Based on the linewidth, a rotational temperature of $\sim$ 1000 K was derived, and the authors concluded that excited SO molecules were ejected from the then very active volcano Loki Patera (de Pater et al., 2002).

More recent observations reveal the spatial distribution of SO, and show that the correlation with volcanoes is tenuous at best (de Pater et al., 2007; 2020). Both the spatial distribution and the spectral shape of the SO emission band vary considerably across Io and over time. In their most recent paper (de Pater et al., 2020), the authors suggest that the emissions are likely caused by a large number of stealth plumes, "high-entropy" eruptions (Johnson et al., 1995) produced through the interaction of silicate melts with superheated SO_2 vapor at depth. These plumes do not have much dust or condensates, and are therefore not seen in reflected sunlight. The SO data are further suggestive of non-LTE processes, in addition to the direct ejection of excited SO from the volcanic vents.

In order to shed more light on the core question whether the dynamics in Io's atmosphere is predominantly driven by sublimation of SO_2-ice or volcanic activity, we present spatially resolved observations of the satellite at 880 μm when Io moved from sunlight into eclipse, and half a year later from eclipse into sunlight. The observations and data reduction are discussed in Section 2 with results presented in Section 3. The analysis of line profiles is presented in Section 4, with a discussion in Section 5. Conclusions are summarized in Section 6.

2. OBSERVATIONS AND DATA REDUCTION

We observed Io with the Atacama Large (sub)Millimeter Array (ALMA) on 20 March 2018 just before and after the satellite moved into eclipse. Similar experiments were conducted when Io moved out of eclipse on 2 and 11 September, 2018. Figure 1 shows the viewing geometry on both occasions. All observations were conducted in Band 7, the 1-mm band. Each continuous observation of a source (calibrator or Io) is referred to as a scan, and gets a scan "label". Amplitude and bandpass calibrations were performed on the radio source J1517-2422 during the first ∼15 min of each of the six ∼35-min long observing sessions (two sessions on each date). The phases were calibrated on J1532-1319 in March and on J1507-1652 in September. These observations or scans (typically 30–60 sec long) were taken before, interspersed, and at the end of the Io observations. Typical Io scans are 6–7 min long, though towards the end of the observing sessions they usually lasted for only 1–2 minutes. The flux densities of J1517-2422 were checked with the ALMA calibrator catalogue; no updates were needed since the observatory's initial pipeline data reduction. On 11 September the flux densities of both Io and the secondary calibrator were much lower for the in-eclipse data than for the ones in-sunlight, perhaps caused by some decorrelation in the phases and/or pointing errors. We therefore multiplied the Io-in-eclipse data by a factor of 1.15, the ratio for the secondary calibrator between the in-sunlight and in-eclipse data sets.

We observed several transitions of SO_2 and SO, and one transition of KCl. These transitions, together with the spectral window (spw) used to observe them, the total bandwidth and channel width of each spw are listed in Table 1. We typically had 3–4 beams (resolution elements) across the satellite. Usually all scans on a particular source are combined to create a map or a spectral line data-cube. Since we are interested in particular in how the spatial brightness distribution and flux density change during eclipse ingress and egress, we imaged individual scans, and even fractions of a scan, as summarized in Table 2.

After the calibration and initial flagging was done in the ALMA pipeline, we split off the Io data into its own dataset (referred to as a measurement set, Io.ms) and attached a new ephemeris file so that the position and velocity got updated every minute of time. We used the Common Astronomy Software Applications package, CASA, version 5.4.0-68 for all our data reduction. This version properly handles the tracking of Io's motion across the sky and velocity along the line-of-sight. Our final products are centered on Io, both in space (images) and velocity (line profiles). We first created continuum maps of the satellite, used initially for additonal flagging and selfcalibration of the data (e.g., Cornwell and Fomalont 1999). Mapping was done using tCLEAN; a model of Io's continuum emission served as a "startmodel" in the deconvolution ("cleaning") and selfcalibration process. The model is a uniform limb-darkened disk with a disk-averaged brightness temperature that matches the data (typically between 65 and 80 K), and a limb-darkening coefficient q =0.3 (i.e., the brightness falls off towards the limb as $\cos\theta^q$, with θ the emission angle). All data were selfcalibrated twice (phase selfcal only), although the second selfcalibration did not improve the data substantially over the first one.

Before creating spectral line data-cubes, we split out each spectral window (Table 1) into its own measurement set (Io-spwx.ms, with x=0–7), and subtracted the continuum emission from each Io-spwx.ms (x=1–7) dataset using the CASA routine UVCONTSUB. At this point we have spectral image data-cubes of just the emission of each species (SO_2, SO, KCl).

In order to create maps of the brightness distribution of each species at a high signal-to-noise (SNR), we averaged the data in velocity over 0.4 km/s, centered at the center of each line; these maps are referred to as "line center maps". To evaluate line profiles, we also constructed 3-dimensional (3D) data-cubes with RA and DEC along the x- and y-axes, and frequency (or velocity) along the z-axis, where each image plane was averaged over 0.142 km/s, which translates roughly into a frequency resolution of ∼160 kHz[2], slightly larger than the 122 kHz width of an individual channel in each spw. All (spectral line, line center, and continuum) maps were constructed using uniform weighting, and cleaned using the Clark or Högbom algorithm with a gain of 10% in CASA's tCLEAN routine. In essence, in this routine we iteratively remove 10% of the peak flux density from that location on the map, together with the synthesized beam (the telescope's antenna pattern). This process is repeated until essentially only noise is left in the "residual" map. These socalled "clean components" form a map, the .model map in CASA. An example is shown in Figure 2. (Note that the continuum maps were deconvolved using a startmodel in tCLEAN, as described above). The .model map is convolved with a circular gaussian beam with a full width at half power (HPBW) that best matches the inner part of the synthesized beam (see Table 2 for the HPBW values) before being added back to the residual map. The .model map in Fig. 2 shows the clean components of the map displayed in the top left panel in Figure 4, discussed below in Section 3.2. We used a cell (or pixel) size for all maps of 0.04", i.e., between 5.5–9 pixels/beam.

[2] Note that the precise number depends on frequency ν, since $\Delta\nu = \nu v/c$, with v the velocity and c the speed of light.

3. RESULTS

3.1. *Continuum Maps*

The continuum maps for each of the 6 sessions, three in-sunlight and three in-eclipse, are very similar, and do not show any structure other than that the maximum temperature is not centered on Io, but slightly displaced towards the afternoon, as shown in Figure 3a,b. We determined the total flux density from such maps, since it is impossible to determine this from the *uv*-data, as these are dominated by the signal from nearby Jupiter. For the maps in-eclipse, the sidelobe patterns from Jupiter produce broad (similar size as Io) low-level (few % of Io's peak intensity) negative and/or positive ripples which affect the precise determination of Io's flux density. Although ideally one would subtract Jupiter from the visibility data, in practice this is not easy as Jupiter is not a uniform disk at mm-wavelengths (e.g., de Pater et al., 2019), moves with respect to Io, is mostly resolved out, and mostly on the edge or outside the ∼20" primary beam. We therefore opted to correct for these negative or positive backgrounds by subtracting the average flux density per pixel as determined from an annulus around Io in each of the 6 maps. Each map was constructed from all scans in the particular observing session, although the in-eclipse scan 6 on 11 September was not used (too much affected by nearby Jupiter).

The total flux density, F_J, normalized to a geocentric distance of 5.044 AU (Io's diameter is 1" at this distance) and averaged over all six measurements, $F_J = 5.43\pm0.15$ Jy, which translates into a disk-averaged brightness temperature, T_b = 93.6±2.5 K. Since Io blocks the cosmic microwave background radiation (CMB), which is 0.044 K at this wavelength, we have added this value to all brightness temperatures quoted. The uncertainties quoted above are the standard deviation or rms spread in the continuum measurements, which is much larger

than the uncertainty in any single continuum measurement based on the rms in the maps, which varies from 0.001–0.008 Jy (0.02–0.14 K) in-sunlight, to 0.008–0.05 Jy (0.14–0.86 K) in-eclipse. For absolute values we need to add the calibration uncertainty in quadrature. A typical calibration error for ALMA data is ∼5%, i.e., the total uncertainty on the brightness temperature is ∼5 K.

For all three dates, there is a small difference between T_b in sunlight and in eclipse: in sunlight we find F = 5.43±0.11 Jy (5.43, 5.39, 5.59 Jy, in chronological order), i.e., T_b = 93.6±1.8 K, and in eclipse F = 5.25±0.14 Jy (5.16, 5.25, 5.44 Jy), i.e., T_b = 90.8±2.2 K. The uncertainties are again the rms spread in the data points. The difference between these numbers, and because all in-eclipse values are lower than the corresponding in-sunlight values, suggests that T_b may decrease by ∼3 K after entering eclipse. This is interesting since at mid-IR wavelengths Io's surface temperature dropped steeply within minutes after entering eclipse (Morrison and Cruikshank, 1973; Sinton and Kaminsky, 1988). Tsang et al. (2016) measured a drop in surface temperature at 19 μm from 127 K to 105 K. At radio wavelengths we typically probe ∼10–20 wavelengths deep into the crust, or ∼1–2 cm at the ALMA wavelengths used (for pure ice this can be hundreds of wavelengths deep). Hence, even after having been in shadow for ∼2 hours, the temperature at depth had decreased by no more than ∼3 K.

The morning-afternoon asymmetry in Io's continuum brightness is also still present during eclipse, or after having been in darkness for ∼2 hrs (Fig. 3b), which further supports our finding that eclipse cooling at depth is slow. We used a simple thermal conduction model (after the infrared version of the de Kleer et al. 2020 model), neglecting albedo variations across Io's surface (which may be reasonable given our relatively low spatial resolution), to demonstrate that the difference between the eclipse cooling at infrared and mm wavelengths can be explained if the upper ∼cm or so of Io's crust is composed of two layers. For the model in Figure 2c we assumed a bolometric Bond albedo, A =0.5, an infrared emissivity ϵ =0.9 and a thermal inertia Γ =50 J m^{-2} K^{-1} s$^{-1/2}$. This number is similar to the value of 70 J m^{-2} K^{-1} s$^{-1/2}$ derived by Rathbun et al. (2004) from *Galileo*/PPR data. At millimeter wavelengths we assumed A =0.5, ϵ =0.78 and Γ = 320 J m^{-2} K^{-1} s$^{-1/2}$. These models, for a "typical" surface location at mid-latitudes, more or less match the data, and suggest that Io's surface is overlain with a thin (no more than a few mm thick) low-thermal-inertia layer, such as expected for dust or fluffy deposits from volcanic plumes, overlying a more compact high-thermal-inertia layer, composed of ice (likely coarse-grained, and/or sintered) and rock. This is very similar to the model proposed by Morrison and Cruikshank (1973) based upon seven eclipse ingress or egress measurements at a wavelength of 20 μm, although our value for the low thermal inertia layer is ∼4 times higher. Sinton and Kaminsky (1988) analyzed 13 observations of eclipse ingress and egress in the early 1980s at wavelengths between 3.5 and 30 μm. They found a best fit by assuming Io to be covered by both dark (A =0.10) and bright (A =0.47) areas, with Γ =5.6 and 50 J m^{-2} K^{-1} s$^{-1/2}$, resp., where the low thermal inertia layer is just a thin layer atop a much higher thermal inertia. They noted that cooling was rapid during the first few minutes, followed by a slower process which they attributed to a combination of the higher thermal inertia, higher albedo passive component and emission from hot spots. Although their thermal inertias are roughly an order of magnitude smaller than the values we found, the overall physical picture of a thin dusty/porous layer atop a more compact high inertia layer is the same for all models. Our millimeter data in particular add a strong constraint to the higher thermal inertia layer roughly a cm or so below Ios surface, a depth not probed at shorter wavelengths. Our values for the upper dusty layer are also similar to those reported for the other galilean satellites (e.g., Spencer, 1987; Spencer et al., 1999; de Kleer et al., 2020), and they agree with the best-fit values found in the thermophysical parametric study by Walker et al. (2012). Note, though, that the latter study, as well as other 2-component thermal inertia studies at mid-IR wavelengths, all refer to horizontal surface variations, while our study refers to a vertically stacked model. In a future paper we intend to expand our 2-layer model to include proper dark and bright surface areas, as done for Ganymede in de Kleer et al. (2020).

3.2. *Line Center Maps (averaged over 0.4 km/s)*

3.2.1. *Line center Maps on 20 March 2018*

SO_2 maps:—Figure 4 (top row) shows SO_2 maps at 346.652 GHz (spw2), averaged in velocity over 0.4 km/s (∼0.45 MHz) centered on the line, from 20 March 2018 when Io went into eclipse. The bottom row shows simultaneously taken SO maps (averaged over both transitions to increase the SNR). The first panel shows Io-in-sunlight, and the next 2 panels show the satellite ∼ 6 min and ∼ 15 min after entering eclipse (Table 2). The large circle shows the outline of Io, as determined from simultaneously obtained images of the continuum emission. As soon as Io enters an eclipse, the atmospheric

and surface temperatures drop (Fig. 3), and SO_2 is expected to condense out on a time scale t $\sim$ H/c_s $\approx$ 70 sec, for a scale height H $\approx$ 10 km and sound speed $c_s \approx 1.5 \times 10^4$ cm/s (de Pater et al., 2002), unless a layer of non-condensible gases prevents complete collapse (Moore et al., 2009). Once in eclipse, assuming complete collapse, the only SO_2 we see should be volcanically sourced. The letters on Figure 4 show the positions of Karei Patera (K), Daedalus Patera (D), and North Lerna (L). Due to the excellent match between the location of these volcanoes and the SO_2 emissions on this day, these volcanoes are likely the main sources of SO_2 gas for Io-in-eclipse. All three volcanoes have shown either plumes or changes on the surface attributed to plume activity in the past (Geissler et al., 2004; Spencer et al., 2007).

SO maps:—SO can be volcanically sourced, i.e., produced in thermochemical equilibrium in the vent (Zolotov and Fegley, 1998), or later via the reaction O + S_2 at a column-integrated rate of 4.6×10^{11} cm^{-2} s^{-1}, or while in sunlight it can be produced through photolysis of SO_2 at a similar column-integrated rate (Moses et al., 2002). About 70% of SO is lost through photolysis into S and O, but during an eclipse the only known loss is through a reaction with itself: 2SO $\rightarrow$ SO_2 + S, at a rate of 3.25×10^{10} cm^{-2} s^{-1} (Moses et al., 2002). Hence, to eliminate an entire column of 10^{15} cm^{-2} (Section 4.3) would take 8.5 hrs, or almost an hour to loose a 10$\times$ smaller column. Hence one would not expect much change in the SO column density upon eclipse ingress. The data, however, clearly show a decrease in the SO emission after eclipse ingress, though not as fast as for SO_2. The observed decrease suggests that SO may be much more reactive with itself than captured by the above reaction rate. Additional (in-between) reactions are: 2SO $\rightarrow$ $(SO)_2$, and SO + $(SO)_2$ $\rightarrow$ S_2O + SO_2 (Schenk and Steudel, 1965). At low temperatures (i.e., in-eclipse), both SO_2 and S_2O condense out, and SO may effectively condense out through chemical reactions in the gas-phase with the surface, producing the above mentioned compounds (Hapke and Graham, 1989). Based on our observations, it looks like such self-reactions of SO must be very fast. Although this possbility has been suggested in the past (e.g., Lellouch, 1996), the SO "condensation" rate has never before been observed.

As shown, the connection with volcanoes is more tenuous for the SO emissions than for SO_2, except perhaps for Daedalus Patera. However, as noted above, SO's column density is not really expected to change much. With a layer of SO, and perhaps other noncondensible species (e.g., O, O_2), SO_2 may indeed not completely collapse, such as modeled by e.g., Moore et al. (2009). We may also see emissions from stealth volcanoes, as postulated by de Pater et al. (2020) to explain the widespread spatial distribution of the 1.707 μm SO emissions, which only occasionally showed a connection to volcanoes.

Disk-integrated flux densities:—We integrated the flux density over Io on each map for each transition (except spw7, the lowest line strength, where we have no detection), and plotted the results on the left panel of Figure 5. For easier comparison, all flux densities in this figure have been normalized to a geocentric distance of 5.044 AU, at which distance Io's diameter is 1". Assuming that Io's flux density is constant while in-sunlight, it decreases exponentially within the first few minutes after the satellite enters eclipse. The dotted lines show the collapse for each transition, modeled for the SO_2 lines as:

$$F_i = F_i(t_0) e^{-t_j/(H_i + C_i(t_j - t_1))} \quad (1)$$

where F_i stands for the flux density in each transition i (for i = spw1, spw2, spw5, and spw6), t_j the time (in min) from time $t_0 = 0$ taken as midway during the partial eclipse, t_1 =8, t_2 = 10.7, t_3 = 19.5 min). H_i shows the exponential decay constant in minutes (indicated on the figure). After the initial drop in intensity, further decrease is slowed down, as roughly indicated by the term $C_i(t_j - t_1)$, with $C = 1$ at 346.524 and 332.091 GHz (spw1, spw5), $C = 0.6$ at 346.652 GHz (spw2), and $C = 0.7$ at 332.505 GHz (spw6). A new "steady state" appears to be reached within $\sim$20 minutes, similar to the results shown by Tsang et al. (2016) at 19 μm. The flux density decreases by a factor of 2 at 346.524, 332.091, and 332.505 GHz (spw1, spw5, spw6), and by 3.2 at the strongest line transition, 346.652 GHz (spw2). As shown by H_i, the latter flux density decreases much faster than the others. Also the SO emission, plotted here as the average of the two transitions, decreases by a factor of 2, although much more gradual, essentially following a linear decay, modeled as:

$$F_i = F_i(t_0) + a t_j \quad (2)$$

where $a = -15$ mJy/min. This more gradual decrease is also visible on the maps in Figure 4.

3.2.2. *Line Center Maps on 2 & 11 September 2018*

2 Sep. 2018—Figure 6 shows the distribution of SO_2 and SO gases on 2 September 2018, when Io moved from eclipse into sunlight. The integrated flux densities are plotted on the right-side panel in Figure 5. As soon as sunlight hits the satellite, SO_2 starts to sublime and

within 10 minutes the atmosphere has reformed in a linear fashion. The flux density in each transition increased by roughly a factor of 2. SO increased by roughly a factor of 3, also in a linear fashion. The dotted lines on the figure were calculated using equ. 2; the values for a in mJy/min (positive sign for increasing slope) are indicated on the figure.

When the satellite was in-eclipse on 2 September (scan 6a in Fig. 6), the spatial distribution of SO_2 gas shows very strong emission near the SW limb, centered on P207 (91^0W long., 37^0S lat.), a small dark-floored patera. Although thermal emission has been detected at this site with the W. M. Keck Observatory (Marchis et al., 2005; de Kleer and de Pater, 2016), no evidence of plume activity has ever before been recorded. Faint emissions can further been seen near Nyambe Patera and just north of PFd1691, a dark-floored patera where thermal emission has also been detected with the Keck Observatory (de Kleer et al., 2019). As soon as Io enters sunlight (scan 6b), the SO_2 emission near P207 becomes more pronounced; this is the side of Io where the Sun first strikes. Over the next 4–5 minutes (scans 8a, 8b) the emissions get stronger, in particular near the volcanoes. At 9 minutes (scan 12) the SO_2 atmosphere has completely reformed.

The bottom row in Figure 6 shows practically no SO emissions while Io is in eclipse (scan 6), except for some emission along the limb north and south of P207. Faint emissions are also seen near PFd1691, and at a few other places on the disk. None of these emissions seem to be directly associated with known volcanoes, nor with the SO_2 emissions on Io-in-eclipse. About 4 minutes after entering sunlight (scan 8) strong SO emission is detected above P207, suggestive of formation through photodissociation of SO_2. Five minutes later we also detect emissions over Nyambe Patera, and another 20–30 min later the SO emissions track the SO_2 emissions pretty well, as expected if the main source of SO is photolysis of SO_2.

11 Sep. 2018—Figure 7 shows the spatial distributions of SO_2 and SO of Io-in-eclipse and in-sunlight on 11 September 2018, but not during the transition from eclipse into sunlight. While in-eclipse, faint volcanically sourced SO_2 emissions are present near P129, Karei and Ra Paterae, and along the west limb near Gish Bar Patera and NW of P207. The eruption at P207, so prominent 9 days earlier, has stopped. No SO emissions are seen above the noise level. Ten minutes later, the atmosphere has reformed as shown by the in-sunlight map, with most of the emissions confined to latitudes within $\sim |30^0 - 40^0|$, in agreement with the latitudinal extent measured from UV/HST data (Feaga et al., 2009), and with Figures 4 and 6. The SO map shows emission peaks above Karei Patera and P129. The ratio of flux densities between in-sunlight and in-eclipse is about a factor of 4–5 for SO_2 and ∼10 for SO on this day (Fig. 5). Hence, as shown both by this large ratio and the maps, on this date there was not much volcanic activity.

3.2.3. *Map of KCl on 20 March 2018*

On 20 March 2018 we also detected KCl, shown in Figure 8. As shown, the distribution is completely different from that seen in SO_2 and SO: the south-eastern spot is centered near Ulgen Patera, and emission is seen along the limb towards the north. There may also be some emission from near Dazhbog Patera. KCl was not detected in September 2018, when Ulgen Patera was out of view. Further analysis of the KCl data will be provided in a future paper.

3.3. *SO_2 Line Profiles and Image Data Cubes (Resolution 0.142 km/s ≈ 160 kHz)*

In addition to the spatial distribution at the peak of the line profiles (i.e., the line center maps) when Io goes from sunlight into eclipse and vice versa, the full image data cubes contain an additional wealth of information.

3.3.1. *Image Data Cubes on 20 March 2018*

In Figure 9 we show several frames of the SO_2 image data cubes together with disk-integrated line profiles from March 2018 for Io-in-sunlight (top half) and in-eclipse (bottom half). To increase the SNR, we averaged the data at 346.524 and 346.652 GHz (spw1 and spw2). We also averaged all scans for the in-eclipse data (Table 2, scans 7–15 in Set 2) in this view.

At the peak of the line profiles (frame 3), the images look similar to those shown in Figure 4. Moving away from the peak we see the SO_2 distribution at a particular radial velocity, v_r (the velocity along the line of sight). It is striking how similar the images are moving towards lower or higher frequencies (positive or negative v_r), i.e., the brightness distribution is very symmetric around the peak of the line. If there would be a horizontal wind of ∼300 m/s in the prograde direction, as reported by Moullet et al. (2008) from maps when Io was near elongation (i.e., a different viewing geometry), we would expect spatial distributions asymmetric with respect to the line center. In the first frame, where we see the spatial distribution of gas offset by $\sim +0.6$ MHz, i.e., moving towards us (blue-shifted – B) at a speed of ∼0.5 km/s ($v_r = -0.5$ km/s), we would expect SO_2 gas on the west (left) limb; we would see the gas on the east limb in frame 5 where we map the brightness distribution at $v_r = +0.6$ km/s. On frame 2 emission would be concentrated on the west hemisphere, and on frame

4 on the east hemisphere. The data show very different spatial distributions. In addition, on frame 5 we see faint emissions on both limbs, i.e, material moving away from us on either side of the satellite, such as expected for day-to-night flows. There is also faint blue-shifted emission along both limbs in frame 1. Hence emissions due to a prograde wind cannot be distinguished in these data.

On frames 1 and 5, both in-sunlight and in-eclipse, emission from near Daedalus Patera dominates. This emission also dominates on frames 2–4 in-eclipse, and is clearly visible in-sunlight as well. Emission from the vicinity of Karei Patera is also visible on frames 2–4 in-eclipse and in-sunlight, as well as on frame 1 in-eclipse. Emission may additionally originate near N. Lerna in several frames. The line profiles, in particular the high velocity wings, are clearly dominated or produced by the volcanic plumes.

3.3.2. *Image Data Cubes on 2 & 11 September 2018*

Figure 10 shows the image data-cube from September 2 when Io moves from eclipse into sunlight. The top half shows the image data cube when Io was in sunlight, and the bottom half shows the results for scan 6 when Io was in eclipse. As for the March data, the broad asymmetric wings of the line profile are clearly produced by volcanic plumes, the plume at P207 on this date.

On 11 September the situation is slightly different, as shown in Figure 11. There were no detectable volcanic plumes. When Io was in-eclipse, only faint SO_2 emissions were seen. At the peak of the line, emissions seem to originate near Euboea Fluctus and Ra Patera. But overall, if SO_2 is volcanically sourced, most faint emissions may be sourced from stealth volcanism, as mentioned in Section 3.2. On the sunlit image data cube we see some emission from the west limb in frame 1, near Zal Patera (northern spot) and Itzamna Patera (southern spot), and on the east limb on frame 5 at Mazda Patera. In frame 2 the emission has shifted more towards the center of the disk, but is still only visible on the western hemisphere, i.e., the side that is moving towards us. In frame 4 more emission is coming from the eastern hemisphere, while in frame 5 emission comes primarily from the eastern limb. These frames could be interpreted as indicative of a ∼300–400 m/s prograde zonal wind (i.e., on top of the satellite's rotation around its axis), although it is not clear why it would be offset from the equator in frame 1. Moreover, such a prograde zonal wind would result in line profiles that are broader than those observed, even when modeled with an atmospheric temperature of ∼ 145 K. Clearly, the spatial distribution on this day is not as symmetric around the center of the line (frame 3) as on the other two dates. On this date most SO_2 must have been produced by sublimation, since we do not see clear evidence of volcanic eruptions in-sunlight nor in-eclipse. This may be the reason that we can distinguish zonal winds such as reported before by Moullet et al. (2008). If these winds are real, they must form within 10–20 minutes after Io re-emerges in sunlight. The reason for zonal winds, if indeed present, remains a mystery, since we would expect day-to-night winds on a body with a warm day- and cold nightside (see, e.g., Ingersoll et al., 1985; Walker et al., 2010; Gratiy et al., 2010).

4. ANALYSIS OF SO_2 AND SO LINE PROFILES

As shown by Lellouch et al. (1990), the SO_2 line profiles as observed are saturated, and the peak flux density depends not only on the temperature and column density, but also on the fraction of the satellite covered by the gas. With our spatially-resolved maps and five observed SO_2 transitions, we should be able to determine the atmospheric temperature, column density and fractional coverage, as well as constrain the presence of winds. This was not possible with any of the previously published observations.

4.1. *Fractional Coverage.*

The fractional coverage of the gas on Io can be determined directly from maps of the SO_2 gas as observed in the various transitions. However, the fractional coverage as seen on such maps (Fig. 4) is significantly affected by beam convolution, which makes it hard to determine the precise fraction. A better way is to use a deconvolved map such as shown in Fig. 2 and discussed in Section 2. The total number of pixels with non-zero intensities divided by the total number of pixels on Io's disk gives us the fractional coverage of the gas over the disk. This procedure works best if the SNR in the maps is high, which is certainly true for the strongest transitions, i.e., 346.652 GHz (spw2), and likely for SO in sunlight (346.528 GHz, spw1), as shown in Figures 4, 6, and 7. The .model files cannot be trusted to accurately represent fractional SO gas coverage in-eclipse, since the signal is so low (hardly above the noise). If the brightness distribution is very flat, like the continuum maps of Io, this procedure underestimates the fractional coverage; it works best if the spatial distribution consists of point-like sources. The fractional coverage, $fr_{\rm map}$, for SO_2 as determined from maps in-eclipse and in-sunlight for all 3 days is summarized in Column 3 of Table 3. We typically see a 30–35% coverage for Io-in-sunlight. On 20 March, ∼15 minutes after entering eclipse, we measured ∼17%, significantly higher than in

September where we measured ∼10% when Io had been in Jupiter's shadow for ∼2 hours. The fractional coverage in-eclipse may primarily depend on Io's volcanic activity, which may vary considerably over time. Interestingly, although there was not much volcanic activity on 11 September, the fractional coverage was quite similar to that measured on 2 September, when P207 was extremely active. This suggests a very vigorous eruption at P207, but small in extent, essentially a point source in our maps. For SO in sunlight we measured $fr_{\rm map}$ ≈16% in March and ∼10% in September. In-eclipse this coverage drops to below ∼5%, and cannot be measured very acurately. We estimate an uncertainty of ∼10% on all retrieved numbers for SO_2, and ∼20% for SO.

4.2. *Radiative Transfer Model*

To model the line profiles, we developed a radiative transfer (RT) code analogous to that used to model CO radio observations of the giant planets (Luszcz-Cook and de Pater, 2013). We assume Io's atmosphere to be in hydrostatic equilibrium, so the density can be calculated as a function of altitude once a temperature is chosen (we use an isothermal atmosphere in this work). Any molecular emissions are assumed to occur in local thermodynamic equilibrium (LTE), as expected for these rotational transitions in Io's atmosphere (Lellouch et al., 1992). We perform RT calculations across Io's disk at a cell size of 0.01" and a frequency resolution 1/4th of the resolution in the observations (i.e., roughly 40 kHz). Io's solid body rotation (v_{rot} = 75 m/s at the equator) is taken into account; a simple increase/decrease in v_{rot} can account for zonal winds.

In order to account for potential Doppler shifts (blue- and red-shifts) in line profiles, which might be expected for localized volcanic eruptions or for day-to-night winds in disk-averaged line profiles, we added a separate parameter, v_r, in addition to the planet's rotation and zonal winds. With this parameter we can accurately fit any offset in frequency at line center. As shown below, we do need the freedom to shift some modeled line profiles to match the data; potential reasons for such shifts are discussed below and in Section 5.

We adopted a surface temperature of 110 K with an emissivity of 0.8. For the analysis of our data we ran many models, where we varied the column density, N, from ∼ 10^{15} – few ×10^{17} cm^{-2} for SO_2, a factor of 10 smaller for SO, the temperature T from∼ 120 – 700 K, and the rotational and Doppler velocities, v_{rot} and v_r, each from ∼ −400 to +400 m/s. In the following subsections we analyze line profiles for March and September.

Figure 12 shows sample contribution functions for the four SO_2 line transitions detected in our data. The line profiles based upon the parameters in panel a) match the observed line profiles quite well, as shown in Sections 4.3 and 4.4. Panels c and d show the changes in the contribution functions when the temperature or column density are changed. Line profiles based upon these parameters do *not* match our observed line profiles, but give an idea where one probes under different scenarios. The column density used in panel d) matches that usually reported for the anti-jovian hemisphere. while the temperature in panel c) is similar to the atmnospheric temperature determined at 4 μm (Lellouch et al., 2015). In panel b we show a calculation for a temperature that increases with altitude, such as expected for Io based upon plasma heating from above (e.g., Strobel et al., 1994; Walker et al., 2010). Resulting line profiles again do *not* match any of our data. The bottom line of this excercise is that we typically probe the lower 10 up to ∼80 km altitudes for column densities of ∼10^{16}–10^{17} cm^{-2}, and that different transitions are sensitive to different altitudes in the atmosphere. We further note that the temperature structure in the first few tens of kilometers above the surface is unknown, which makes interpretation of mm-data quite challenging.

4.3. *SO_2 on 20 March 2018: Sunlight → Eclipse*

4.3.1. *Disk-integrated line profiles.*

We first focus on the disk-integrated line profiles of SO_2 for Io-in-sunlight. We have 5 transitions; although there essentially is no signal in the weakest line transition (333.043 GHz, in spw7), it still helps to constrain the parameters. The free parameters in our model are N_t, T_t, fr_t, v_{rot} and v_r, where the subscript t is used for disk-integrated data. We thus have to find a set of parameters that can match the line profiles in all SO_2 transitions. Moreover, since the fractional coverage, fr_t, should match that derived from the maps, $fr_{\rm map}$ (Table 3), the parameter fr_t is heavily constrained for disk-integrated line profiles.

While the Doppler shift, v_r, in our implementation leads to a shift in frequency (i.e., velocity) of the entire line profile, both the temperature and rotation of the body (or any zonal wind), v_{rot}, lead to a broadening of the line profile. Hence high values of v_{rot} can be compensated by lower atmospheric temperatures. For example, for v_{rot} =300 m/s and T_t =195 K, the lineshape matches the observed profiles quite well; however, for any given N_t, there is not a single value for fr_t that can match the line profiles for all transitions; moreover, fr_t should be equal to $fr_{\rm map}$. Based upon such comparisons we can rule out zonal winds much larger than ∼100 m/s, which agrees with our earlier findings where we did not

see evidence on the maps for large zonal winds, except perhaps for September 11 (Section 3.3). Since there is no noticeable broadening in the line profiles for zonal winds up to ∼100 m/s, we ignore any potential presence of zonal winds in the rest of this section, and simply use v_{rot} = 75 m/s.

By assuming that the fractional coverage of SO_2 on Io, fr_t, should be the same for all transitions, and be equal to $fr_{\rm map}$, we get a pretty tight constraint on the column density and atmospheric temperature: $N_t = (1.35 \pm 0.15) \times 10^{16}$ cm^{-2} and $T_t = 270\pm^{50}_{25}$ K. These numbers are summarized in Table 3, together with fr_t; the spread in fr_t between transitions is written as an uncertainty.

We found that the modeled profile had to be shifted in its entirety by +20 m/s (22–23 kHz), with an estimated error of 7 m/s. Since uncertainties in the line positions as measured in the laboratory are of order 4 kHz[3], the observed offset cannot be caused by measurement errors in the lab. This shift is indicative of material moving away from us. This can be caused by an asymmetric distribution of the gas with more material on the eastern than western hemisphere. Alternatively, it can be caused by day-to-night flows, or gas falling down onto the surface such as expected in volcanic eruptions after ejection into the atmosphere. The rising branch of gas plumes usually occurs over a small surface area (vent), is very dense (∼few 10^{18} cm^{-2}; see, e.g., Zhang et al., 2003), and therefore saturated. While rising, the plume cools and expands, and the return umbrella-like flow, essentially along ballistic trajectories, covers a much larger area, up to 100's km from the vent, with column densities about 2 orders of magnitude lower than at the vent. Hence, since the downward flow covers a much larger area than the rising column of gas, one can qualitatively explain a redshift of disk-integrated line profiles. This idea was used by Lellouch et al. (1994; see Lellouch, 1996 for updates) to explain ∼80 m/s redshifts in their line profiles, which they could model if there would be of order 50 plumes on the observed hemisphere. Although this seemed quite a large number of plumes at the time, if one considers the presence of stealt plumes (Johnson et al., 1995) and the recent publication of the spatial distribution of 1.707 μm SO emissions (de Pater et al., 2020), this may be a quite plausible idea.

Several fits are shown in Figure 13, panels a and c. For each of the models shown we used the mean fractional coverage as derived from the line profiles in the four spectral windows (spw1, spw2, spw5, and spw6) for that particular model, i.e., fr_t = 0.32 for the best-fit model ($N_t = 1.35 \times 10^{16}$), but fr_t =0.39 for $N_t = 1 \times 10^{16}$ cm^{-2} and fr_t =0.26 for $N_t = 2 \times 10^{16}$ cm^{-2}. While all three model curves might match one or two spectral windows, only one curve (red one) fits all transitions, as well as $fr_{\rm map}$. Note, though, that none of the curves fits the broad shoulders of the observed profiles; this is clearly caused by the relatively high velocities (Doppler shift) of the eruptions, as discussed in Section 3.3 and Figure 9.

The column density and temperature hardly change for Io-in-eclipse (scan 11+15) (Table 3). The drop in flux density is mainly caused by the factor of ∼2 drop in fractional coverage. In other words, a smaller fraction of the satellite is covered by gas, but over those areas the column density and temperature are essentially the same as those seen on Io-in-sunlight. Line profiles are shown in panels b and d of Figure 13. We note the discrepancy between the data and models in panel d, indicative of shortcomings in our model: while the line profiles of Io-in-sunlight can be modeled relatively well with our simple hydrostatic model, the model falls short when the gas emissions are dominated by volcanic plumes rather than by SO_2 sublimation. In this particular case there appears to be excess emission at lower frequencies, i.e., at velocities moving away from us.

4.3.2. *Line profiles for individual volcanoes.*

We next investigate the line profiles of individual volcanoes, Karei and Daedalus Paterae. These line profiles were created by integrating over a circle with a diameter equal to the HPBW (Table 2) centered on the peak emission of the volcano on the 346.652 GHz (spw2) map. We determined the line profile for the models in the exact same way, so that the rotation of the satellite was taken into account, and the viewing geometry (i.e., pathlength through the atmosphere) was the same. Hence, the modeled line profile for a volcano on the West (East) limb is already Doppler shifted to account for the satellite's rotation towards (away from) us, and any additional shifts are intrinsic to the volcano itself. As shown, the hydrostatic line profiles match the observed spectra for Karei Patera in sunlight very well (Fig. 13e) with a column density and temperature that are quite similar to the numbers we found for the integrated flux densities, but with a fractional coverage of almost 50% (Table 4). Hence, the column density (cm^{-2}) of SO_2 gas in-sunlight appears to be quite constant across Io over areas where there is gas, i.e., over approximately 30–35% of Io's surface in-sunlight, and over about half the area of a volcanically active source (note that we integrated here over approximately the size of the beam, so the plume itself may be unresolved).

[3] https://spec.jpl.nasa.gov

Since we cannot determine the fractional coverage for individual volcanoes from the maps, we have to solely rely on finding models that give us the same fractional coverage in all four transitions. The uncertainty in fr_v (the subscript v stands for volcano) as listed in Table 4 shows the spread in fr_v between the four transitions. If the spread is small, the solution is quite robust. When the spread is large, the results should be taken with a grain of salt. The line center is offset by +60 m/s, indicative of material moving away from us, such as might be expected for an umbrella-shaped plume as discussed above. The in-eclipse profile (panel f) can also be matched quite well, with a similar temperature, perhaps a higher column density, but a much lower fr_v.

The observed profile for Daedalus Patera in-sunlight is very different. The profiles in all four transitions have a pronounced red wing (Fig. 13g). The main profile can be matched quite well with $T_v \approx 220$ K, and $N_v \approx 1.5{\times}10^{16}$ cm^{-2}, with a fractional coverage of 46%. The line center appears to be Doppler shifted by −40 m/s, i.e. material moving towards us. Note that the line offsets for the two volcanoes are in the direction of a retrograde, rather than prograde, zonal wind; however, if such a wind would prevail, we would expect the windspeed to be largest near the limb (Daedalus Patera), i.e., opposite to the observations. The observed Dopplershifts are more likely local effects, produced by the eruptions. For the in-eclipse profile (Fig. 13h) no good solution could be found, as indicated by the large uncertainties. This is not too surprising, since in-eclipse most emissions are likely volcanic in origin, since as soon as SO_2 gas is cooled to below its condensation temperature it may condense out. The applicability of our simple hydrostatic model is therefore limited. To properly model these one needs to add volcanic plumes to the model, such as done by e.g., Gratiy et al. (2010). (see also Section 5.3).

4.4. *SO_2 on 2 & 11 September 2018: Eclipse → Sunlight*

Figure 14 shows several line profiles for the September data; best fits are summarized in Tables 3 and 4. As with the March data, the disk-integrated line profiles for both 2 and 11 September for Io-in-sunlight can be modeled quite well with our simple hydrostatic model, in contrast to line profiles taken of Io-in-eclipse where emissions must be volcanic in origin, and the applicability of our model is limited. From our hydrostatic models we find that the SO_2 fractional coverage on both days is a factor of 3 lower for the in-eclipse data than for Io-in-sunlight, while it was only a factor of 2 in March. On the latter date the satellite had only been in shadow, though, for 15 minutes, much shorter than for the September data. While on 11 September the column density between in-sunlight and in-eclipse data is very similar, on 2 September it may be a factor of 2 higher when in-eclipse, although the uncertainties are large enough to accommodate no-change as well.

Line profiles of individual volcanoes, calculated by integrating over a circle with a diameter equal to the HPBW, also deviate significantly from the hydrostatic models, although for volcanoes in-sunlight the discrepancies are smaller than when in-eclipse. We were able to find a good model for P207, in particular in-sunlight, where a column density quite similar to that found for the disk-integrated line profiles covers ∼60% of the volcano. During eclipse the fractional coverage decreases by a factor of ∼2 (or more), while the column density may not vary much (considering the uncertainties). In contrast, even though the observed line profiles for Nyambe Patera look quite gaussian both in-sunlight and in-eclipse, we were not able to find a model for either data set with the same fr_v for all 4 transitions, which translates into a high uncertainty even for the in-sunlight data.

4.5. *SO Line Profiles*

We modeled the disk-integrated SO line profiles in Figure 15 by adopting the temperature that was determined from the SO_2 profiles on the various days, since the atmospheric temperature should not depend on the species considered. The fractional coverage as determined from the line center maps for Io-in-sunlight is about a factor of 2 lower for SO than for SO_2 in March, and more like a factor of 3–4 in September. The temperature together with this fractional coverage should result in a trustworthy value for the column density, assuming again that the atmosphere is in hydrostatic equilibrium. With these assumptions we find a column density of $\sim 10^{15}$ cm^{-2} on 20 March when in-sunlight, roughly a factor of 10 below the SO_2 column density. This, with the lower fractional coverage, suggests a difference of a factor of ∼20 between the total volumes of SO and SO_2 gas, in good agreement with previous observations (e.g., Lellouch et al., 2007). On 2 September the column density is roughly a factor of 5 lower than the SO_2 column density, which with the much lower fractional coverage also suggests almost a factor of 20 difference in gas volumes. On 11 September the column density is again a factor of 10 below the SO_2 value, but with a much lower fractional coverage this results in a difference of ∼40 between the volumes of SO_2 and SO gases.

As shown in Figures 4, 6, 7 and 15 we did detect SO when Io was in-eclipse in March and on 2 September,

but not on 11 September. The SNR in the maps, however, is very low, which prevented a good estimate of the fractional coverage, a necessary quantity to determine the column density from the data. Assuming the same temperature as derived from the SO_2 maps for Io-in-eclipse, we find a fractional coverage of 7% for an SO column density of 10^{15} cm^{-2}, i.e., about half the fractional area for the same column density as seen in the in-sunlight maps. The fractional coverage decreases for a higher value of N_t, and vice versa for a lower value. On 2 September the most likely scenario for Io-in-eclipse is that both fr_t and N_t decrease by a factor of 2, while on 11 September no SO emissions were detected in-eclipse.

5. DISCUSSION

5.1. *Summary of Observations*

We observed Io with ALMA in Band 7 (880 μm) in five SO_2 and two SO transitions when it went from sunlight into eclipse (20 March 2018), and from eclipse into sunlight (2 and 11 September 2018). On all three days we obtained disk-resolved data cubes, and analyzed SO_2 and SO line profiles for both the disk-integrated data, and for several active volcanoes on the disk-resolved data cubes. Specifics on the observations and derived parameters are summarized in Tables 1–4.

5.1.1. *Disk-integrated data: SO_2*

The line-emission disk-integrated flux densities[4] are typically $\sim 2-3\times$ higher for Io-in-sunlight than in-eclipse (Fig. 5), indicative of a roughly 30–50% contribution of volcanic gases to the SO_2 emissions. However, there is much variability in these numbers. On 11 September the SO_2 flux density in-sunlight is 4–5 times higher than in-eclipse. In March, when Io went into eclipse, the flux density in the strongest transition, $F_{346.652}$, dropped exponentially by a factor of 3, in contrast to the factor-of-2 drop in the three weaker transitions. $F_{346.652}$ for Io-in-sunlight was $\sim 2\times$ higher than $F_{346.524}$, about 30% above the ratio in their intrinsic line strengths (Table 1). In contrast, the observed ratios between $F_{346.524}$ with $F_{332.091}$ and with $F_{332.505}$ are 40 and 60% smaller than the ratios between their intrinsic line strengths. Since the flux density in the various transitions depends also on the atmospheric temperature, which determines (in LTE) which energy levels in the molecule are populated (Boltzmann's equation), the differences in flux density between the various transitions was used in Section 4 to determine the column density and atmospheric temperature. For example, for lower temperatures, the modeled $F_{346.652}$ would be too low, while the modeled $F_{332.505}$ would be too high, which can be qualitatively understood from the difference in contribution functions between panels a and c in Figure 12. We found that neither the atmospheric temperature nor the column density between the in-sunlight and in-eclipse data sets did noticeably change, but that the differences in flux density could be accounted for by a factor of 2–3 decrease in fractional coverage. Or in other words, the column densities (cm^{-2}) remained the same, but there were fewer areas (2–3 times less) above which SO_2 gas was present.

Tsang et al (2016) measured a factor of 5±2 drop in column density when Io moved from sunlight into eclipse. However, since they cannot distinguish between a high column density with low fractional coverage and a low column density with a high fractional coverage, our findings essentially agree.

All observations could be matched quite well with an isothermal atmospheric temperature of 270±50 K. This is clearly an oversimplification, since the temperature will certainly vary with altitude, and also with latitude, longitude, and time of day. Walker et al. (2010) show that the atmospheric (translational) temperature rises steeply with altitude due to plasma heating from above. Near the surface the SO_2 gas is expected to be in equilibrium with the surface frost, rising to ∼400 K at an altitude of 70 km during the day; at night the plasma can reach lower altitudes so that the 400 K temperature may be reached at an altitude of ∼40 km. The exact 3D temperature profile depends on the 3D distribution of the atmospheric density, which for SO_2 is tightly coupled with the frost distribution and temperature. Moreover, as seen from the previous sections, volcanic plumes may affect the atmosphere and its temperature structure quite dramatically. We will get back to this in Section 5.3. The bottom line is that altitude-dependent changes in temperature and density affect the various transitions in different ways, as shown by the contribution functions in Figure 12.

In contrast to the exponential decrease in intensity during eclipse ingress, there is a linear increase during egress for at least about 10 minutes. Interestingly, the SO_2 flux density in three of the four transitions $\sim$ 10 minutes after emerging from eclipse on 2 September is higher than the values 1/2 hr later: 4±2.6% higher for $F_{346.652}$, 16±7% for $F_{332.091}$ and 19±7% for $F_{332.505}$.

The disk-integrated flux densities for September 11 are shown alongside the September 2 numbers in Figure 5. The in-eclipse flux densities for SO_2 on Sep. 11 are typically a factor of 2 (two strongest transitions) – 3 (two weakest transitions) below the Sep. 2 in-eclipse

[4] The disk-integrated flux densities are normalized to a geocentric distance of 5.044 AU for intercomparison of the datasets.

values. As shown in the line center maps, on Sep. 11 the volcanic acitivity was very low, which may explain the difference in flux densities between these dates. When in sunlight, the Sep. 11 numbers for SO_2 are well below the Sep. 2 values, in particular for the two weakest transitions, which are lower by a factor of 1.18±0.09 at 332.091 GHz, and 1.29±0.09 at 333.043 GHz, compared to the nearby high Sep. 2 values.

Since all SO_2 at temperatures below its dew point (i.e., near the surface) condenses out, only gas sourced from volcanic vents, or SO_2 gas that was prevented from complete collapse by a layer of non-condensible gases (e.g., Moore et al., 2009) can be present on Io-in-eclipse. These gases apparently cover ∼10%, and at times up to almost 20% of Io's surface. In some cases there is a clear connection to a particular volcanic eruption; in other cases emissions from volcanically-sourced gases could be caused by stealth volcanism, which presence had been postulated to explain the 1.707 μm forbidden emissions on this hemisphere (de Pater et al., 2020). Point sources and glows of gases that were seen on this hemisphere with the New Horizons spacecraft, interpreted as being caused by plasma interactions with the (near-)surface (Spencer et al., 2007), could also be a signature of stealth volcanism (de Pater et al., 2020).

5.1.2. *Disk-integrated data: SO*

The SO flux density for Io-in-sunlight is highest on Sep. 2 (0.66±0.03 Jy) and lowest on Sep. 11 (0.45±0.04 Jy). Despite the fact the SO is not expected to significantly decrease during an eclipse (Section 3.2), we see a gradual (linear) decrease by a factor of 2 in March. Since SO does not condense at these temperatures, it is likely removed from the atmosphere through reactions with itself on the surface, at a much faster rate than hitherto anticipated (Section 3.2). SO similarly is restored much more slowly than SO_2, indicative of formation from SO_2 through photolysis. According to Moses et al. (2002), SO is formed through photolysis of SO_2 at a column abundance rate of 4.6×10^{11} cm^{-2} s^{-1}; i.e., it takes about 1/2 hr to produce a full column of $\sim10^{15}$ cm^{-2} s^{-1}, and less depending on how much SO gas is left. Above volcanoes, about 50% of SO is produced this way, and another 50% may be produced at a similar rate through the reaction of $O+S_2$. The data (Figure 5) show that SO is fully restored within ∼10 min of time, which given the uncertainties in the ALMA column densities, and the various processes to produce SO (Section 3.2), agrees pretty well with the models.

5.1.3. *Disk-resolved data and line profiles*

On 20 March the SO_2 emission is dominated by the volcanically active Karei and Daedalus Paterae, while some low-level emission is seen near North Lerna. On 2 September the emission is dominated by P207, while we also see emission near PFd1691 and Nyambe Patera. The situation is less clear on 11 September: P207 Patera was no longer active, while emissions on Io-in-sunlight were seen above Karei and Nyambe Paterae. In-eclipse very low-level activity was seen over Karei, Gish Bar, Ra and P129 Paterae, north of P207, and near Euboea Fluctus. SO emissions in March tracked the SO_2 emissions reasonably well, i.e., both Karei and Daedalus Paterae showed activity. On 2 September no clear SO emissions were seen during eclipse, but ∼4 minutes after Io emerged from eclipse SO emissions were detected over P207 and near Nyambe Paterae. On 11 September no SO emissions were detected in-eclipse; when Io was in-sunlight SO emissions were highest over Karei Patera, and visible above P129, and faintly across the equatorial band, more or less coinciding with the SO_2 emissions. This all suggests that the main source of SO is photolysis of SO_2. As mentioned above, at volcanic eruption sites a full column of $\sim10^{15}$ cm^{-2} s^{-1} will be produced in 15 min. The SO peak intensity levels above P207 changed from $\lesssim$0.04 Jy/bm in-eclipse (sc.6, Fig. 6), to ∼0.07 Jy/bm (sc. 8) to ∼0.12 Jy/bm in-sunlight. Hence in ∼4 min photochemical reactions likely produce enough SO to explain the observations.

The effect of volcanoes on the SO_2 and SO emissions is most clearly seen in the lineshapes. While disk-integrated Io-in-sunlight data can usually be matched quite well with hydrostatic models, the in-eclipse profiles deviate considerably from such gaussian-shaped profiles. Both in-sunlight and in-eclipse disk-integrated line profiles show broad low-level wings out to ∼1 MHz from line center, indicative of velocities of order 800–900 m/s both towards and away from the observer. As shown on Figures 9 and 10, these wings are clearly caused by volcanic plumes.

The line profiles for individual volcanoes often show red- or blue-shifted wings, while on some occasions the entire profile seems to be shifted towards lower or higher frequencies. In particular in March, the SO_2 line profile of Karei Patera showed a +60 m/s shift, and a −40 m/s shift for Daedalus Patera, while the disk-integrated line profiles were redshifted by +20 m/s. Based upon our earlier discussions, the redshifts may be caused by the plume above Karei Patera, where ejection of the gas is confined to a small (unresolved) area, while the plume material falls back down on the surface over a much larger area, 100's of km in radius, resulting in a redshift in the line profile. Daedalus Patera, showing a blueshift (which in part offsets the redshift in the disk-integrated line profile), must be dominated by material

moving towards us. Daedalus, in contrast to Karei Patera, is located very close to Io's limb (Fig. 4), and hence is seen under a very different viewing geometry such that both the rising plume material, but also part of the umbrella-shaped plume, is moving towards us, resulting in a blueshift of the entire profile. The redshifted wing on the volcano's line profile is still indicative of material falling down onto the surface, away from us, much of it perhaps over the limb.

The emission over P207 is also on the limb of the satellite, but here we see a wing of blueshifted material while there is no noticeable offset of the entire profile. Clearly, both the viewing geometry and the exact geometry or shape of the plume and ejection itself, in combination with overall windflow patterns (e.g., Gratiy et al., 2010), are important parameters that affect the line profile.

5.2. *Post-eclipse Brightening*

As mentioned above, the flux density on 2 September ∼10 minutes after emerging from eclipse was considerably higher, up to ∼20% in some transitions, than 1/2 hr later. This appears to be an anomalous post-eclipse brightening effect. A ∼10% brightening of the satellite for about 10–20 min after emerging from eclipse was first reported by Binder and Cruikshank (1964) at a wavelength of 450 nm, i.e., they observed the satellite's surface in reflected sunlight. The authors noted that Io was ∼10% brighter when it emerged from eclipse, which decreased over the next ∼15 minutes. They suggested that the brightening might be caused by an atmospheric component that condenses on Io's surface during the eclipse. This makes the satellite bright; the ice should evaporate only minutes after receiving sunlight again, resulting in a slow darkening, back to its original reflected-sunlight intensity. We note that these observations were obtained before Io's atmosphere and its volcanic activity were detected – in fact, based on their data, the authors suggested Io to have an atmosphere. During subsequent years, both detections and non-detections (e.g., Cruikshank et al., 2010; Tsang et al., 2015) of this "post-eclipse brightening" effect have been reported at wavelengths from the UV to the mid-IR. Explanations of the effect range from condensation with subsequent sublimation of SO_2-frost (Binder and Cruikshank, 1964; Fanale et al., 1981; Belluci et al., 2004), to changes in Io's reflectivity due to sulfur allotropes as a result of changes in surface temperature (Hammel et al., 1985), to interactions of amospheric molecules with Jupiter's magnetospheric plasma (Saur and Strobel, 2004). Some authors concentrate on phenomenae causing a brightening of the surface, and others of the atmosphere. No clear explanation has been provided yet; and as shown by the data, the effect has not always been detected, which has been interpreted by possible differences in frost coverage at different longitudes.

The gradual increase in flux density in our data during the first ∼10 minutes after emerging from eclipse into sunlight is exactly how Binder and Cruikshank (1964) explained their observed post-eclipse brightening of Io's surface: The surface was bright since the SO_2-ice coverage had increased due to condensation while in eclipse; as soon as the surface warmed, SO_2 sublimed, the satellite's surface darkened, and the atmosphere reformed. The situation, as we observed it, is a bit more complex in that we see the SO_2 flux density to "overshoot" after 10 minutes (the end of our observing session 1 on Sep. 2), before reaching a steady state (in observing set 2 on Sep. 2). In the next section we show that this may result from the interaction of volcanic plumes with the reforming atmosphere.

5.3. *Comparison of Data with Atmospheric Models*

5.3.1. *Summary of Published Plume Simulations*

In the following we compare the above results with simulations of volcanic plumes by Zhang et al. (2003) and McDoniel et al. (2017). These simulations include a full treatment of gas dynamics, radiation (heating and cooling through rotational and vibrational radiation), sublimation and condensation. McDoniel et al. (2017) coupled Zhang et al.'s (2003, 2004) original plume model to a model of a sublimation-driven atmosphere, developed over the years by Moore et al. (2009) and Walker et al. (2010, 2012). Simulations with this coupled model show how a volcanic plume on the dayside expands in a sublimating atmosphere. The authors present models for a Pele-type plume both on the night and day side. They assumed a night side surface temperature of 90 K, and 116-118 K during the day. The gas erupts from the vent at a temperature of ∼600 K and a source rate of $\sim 10^{29}$ SO_2 molecules/second at hypersonic velocities of close to 1 km/s. It then expands and cools. At an altitude of ∼300 km a canopy-shaped shock forms (due to Io's gravity field) where the radially expanding molecules turn back down to the surface. Most of the gas falls down ∼400–600 km from the vent. On the night side, the SO_2 gas condenses and forms a ring around the volcano which matches the red ring observed around Pele. Due to plume expansion and vibrational cooling the gas temperature above the vent decreases to very low (∼50 K) temperatures, while the temperature in the canopy-shock is of order 300–400 K.

On the night side the model shows an average column density $N_v = 1.1 \times 10^{16}$ cm^{-2} over a region up to ∼600 km from the vent. Directly above the vent, though,

$N_v \approx 10^{18}$ cm^{-2}, and drops by an order of magnitude over a 30-km distance.

A Pele-type plume on the day-side is different because there is also SO_2 sublimation from Io's surface, and hence the plume expands in a background atmosphere. The extent to which a dayside sublimation atmosphere is affected by plumes depends on the size, density and ejection velocity of the plume, as well as on the density of the sublimation atmosphere, which is set by the temperature of the surface frost (for details, see McDoniel et al. 2017). Plumes that do not rise up above the exobase (i.e., the altitude at which the mean free pathlength between collisions is equal to one atmospheric scaleheight, which is typically at an altitude of ∼30–50 km on Io – McDoniel et al., 2017), will not affect the atmosphere very much. Once a plume rises above the exobase, like a large Pele-type plume, it will produce a canopy-shock similar to that on the night-side. However, whereas at night the gas falls down and hits the surface, during the day it will encounter the atmosphere, and a re-entry shock develops. This will heat the atmosphere up to levels similar to or higher than that seen at the vent. The resulting high temperature will lead to excess frost sublimation, which gets entrained in the plume flow. Due to the high pressure created by the high temperature, material will be pushed away, which actually results in a decrease in the column density at the intersection between the canopy and the atmosphere (i.e., where at night the red ring around Pele was created). Some of the material falling down onto the atmosphere creating the re-entry shock, will "bounce" once, or perhaps multiple times, back up and outwards, forming re-entry shocks everytime when falling down onto the atmosphere (compare, e.g., the bounces on the atmosphere seen during the Comet Shoemaker-Levy 9 impact; Nicholson et al., 1995). This expands the area of the plume's interaction with the atmosphere by factors of 2–3. The bounces and outward expansion are more pronunced at higher surface temperatures and atmospheric densities. Because ultimately the temperature of the surface frost will maintain the hydrostatic atmosphere in vapor pressure equilibrium, the total mass in the lower atmosphere may not change much, but large amounts of plume material may displace the originally "sublimed" gas. The total mass of material in the plume area will be enhanced, though it is not a simple addition of the sublimated atmosphere and the plume material ejected in the absence of a sublimation atmosphere (only 60–75% of such a nightside plume is added to the sublimation atmosphere).

5.3.2. *Comparing ALMA Data with Atmospheric Simulations*

Sublimation atmosphere:—During eclipse ingress in March the SO_2 flux density decreased exponentially, caused by a decrease in the volume of SO_2 molecules (assuming a hydrostatic atmosphere we showed that the column density and temperature did not change much; only the fractional area decreased). With such a tenuous atmosphere, one would expect the surface temperature to drop instantaneously when entering eclipse, as shown to be true by Tsang et al (2016). Given a diffusion time of 70 sec (Section 3.2.1; de Pater et al., 2002), the SO_2 molecules are expected to rapidly condense onto the surface, which means that the number density of molecules just above the surface decreases, resulting in a downward motion of gas above it. Moore et al. (2009) show that changes occur primarily in the bottom 10–20 km. They further show that even a small amount of non-condensible gases will form a diffusion layer near the surface. Once this layer is several mean-free path-lengths thick, it will prevent or at least slow down further collapse of the SO_2 atmosphere. They predict this to happen after about 20 min. They also predict that in this case the gas column density and the atmospheric temperature remain essentially the same. In their calculations they assumed, though, that SO is non-condensible, while our data show that SO in essence rapidly condenses through self-reactions on the surface (the flux density or volume of SO molecules decreases linearly at a rate of 15 mJy/min). However, since our observations show essentially no change in column density and temperature, and some SO_2 gas is always present, even when volcanic activity is low (Fig. 11), atmospheric collapse may indeed be retarded by a diffusive layer of non-condensible gases near the surface. We cannot exclude the possibility of SO_2 emissions due to stealth volcanism, however.

During eclipse egress in September both the SO_2 and SO emissions increase linearly, though SO is clearly delayed compared to SO_2, which we attributed to formation through photochemistry (Section 5.1.2). The atmosphere is restored within about 10 min after re-emerging in sunlight. This suggests that the surface heats up essentially instantaneously, causing SO_2-ice to start to sublime immediately. This is very different from the calculations by Moore et al. (2009), who show the atmosphere to reform on a much ($\gtrsim 3\times$) longer timescale.

Volcanic plumes:—The beamsize in our data is ∼1200 km, which is similar to the plume extent of Zhang et al.'s (2003) simulated Pele-type plume at night. A dayside Pele-type plume, though, when including the effect of bounces, would be resolved in our data. On 2 September, when Io was in eclipse after having been ∼2 hours in the dark, the volcanic plume over P207 was quite

bright, and the line profile very asymmetric (Fig. 14) with a strong blue-shifted component, indicative of material moving in our direction. Such a line profile would be expected from Zhang et al.'s (2003) models, as shown by Moullet et al. (2008), who calculated line profiles based upon these models at different locations on Io's disk. Depending on the exact geometry of the plume, they find kinks or shoulders in the line profile, not unlike what we observed for P207. The blue-shifted shoulder is caused by the umbrella-shaped plume material, seen on the limb, moving in our direction. The model also predicts velocities v_r of order 700 m/s, which agrees well with the wings in our disk-integrated line profiles, which are caused by the plumes (Figs. 9,10).

Within 1–2 minutes after emerging in sunlight, the P207 plume increased in intensity, and continued to increase for the next several minutes (Fig. 6). During this period, the plume transitions from a night-side plume to a day-side plume, when SO_2 sublimation from SO_2 frost becomes important. McDoniel et al. (2017) show calculations of a plume transitioning from the night to the dayside, and back into the night, a process that takes almost a full Io day (42.5 hrs). The ALMA observations, in contrast, show a very accelerated process since eclipse egress only takes a few minutes. During these few minutes, SO_2 frost starts to sublime and the atmosphere reforms, while the volcano continues to eject gases. The plume starts to interact with the atmosphere while it is forming. A re-entry shock forms where the plume material hits the atmosphere. The resulting high temperature (Section 5.3.1) accelerates SO_2 sublimation, which gets entrained in the plume flow, causing the plume area to grow. Hence, the observed brightening and expansion of the SO_2 emissions near volcanic vents, i.e., near regions where we see some (though sometimes faint) SO_2 emissions during eclipse is consistent with McDoniel et al.'s simulations. It may also cause the post-eclipse brightening effect we see about 10 min after eclipse egress, where the sudden change from night to day and the interaction of the plume with the reforming atmosphere may lead to a temporary "excess" in SO_2 emissions, likely due to an altitude-dependent temporary increase in atmospheric temperature.

The authors further show that the average column density over the vent at night is $\sim 10^{16}$ cm^{-2}, and that during the day the column density over the plume matches that over the dayside hemisphere at distances $\gtrsim 150$ km. This essentially agrees with our observations, where column densities over the plume and background atmosphere on the dayside are very similar. The differences in brightness we see between the day- and night-(eclipse) side, both disk-averaged and over volcanoes, are mostly explained by changes in the fractional area covered by the gas, but columns of gas over these areas are very similar. Given our relatively low spatial resolution this may well be consistent with the models.

The temperature that best matches our line profiles, ∼220–320 K, can be explained qualitatively by the various temperatures expected along the line-of-sight through the model, which varies from ∼50 K above the vent up to 300–400 K at the canopy shock. For comparison, when Moullet et al. (2008) parameterized the Zhang et al. (2003) night-side plumes at a location ∼40° away from disk center, they found that the models could be mimicked well with an isothermal temperature of ∼190 K. However, given how complex the plume–atmosphere interaction is (McDoniel et al., 2017), we do not think that the atmosphere can be modeled correctly using a simple isostatic atmosphere.

In March we detected vigorous eruptions at Karei and Daedalus Paterae. At Karei Patera the fractional coverage in sunlight was roughly 3 times larger than in eclipse, with an atmospheric temperature of 270±50 K both in sunlight and in eclipse. As mentioned before, the entire profile was redshifted by 60 m/s, while in eclipse the profile was slightly skewed, peaking more at the blue side of the spectrum. The overall shift towards the red is indicative of plume material falling back down onto the surface, away from us; since the umbrella-shaped plume is much larger in extent than the rising column of gas, this can qualitatively explain the line profiles.

Daedalus Patera, in contrast, shows a strong red-shifted shoulder, somewhat similar to the blue shifted shoulder for P207 in September. The entire profile was slightly blueshifted, presumably because the umbrella-shaped plume material from a volcanic ejection near the limb has a large component of material moving towards us (i.e., similar to the material that explains the blue-shifted wing of the line for P207). The red-shifted wing, though, shows that a large component of plume material is also moving away from us.

When Moullet et al. (2008) modeled the Zhang et al. plumes for comparison with their radio data, they did not see such red-shifted shoulders in the models. This, together with our observations of line profiles that are very asymmetric, in particular in-eclipse, shows that the volcanic eruptions are much more complex than the Zhang et al. (2003) and McDoniel et al. (2017) models predict. This is not too surprising; volcanic eruptions are likely not axisymmetric, and may fluctuate in ejection speed, direction, and gas content on timescales much shorter than we can capture in our observations. Yet, it is re-assuring that our observations do qualitatively match many features in the model.

6. CONCLUSIONS

We used ALMA in Band 7 (880 μm) to observe Io in five SO_2, two SO, and one KCl transitions when it went from sunlight into eclipse (20 March 2018), and from eclipse into sunlight (2 and 11 September 2018). We summarize the main findings as follows:

• The disk-averaged brightness temperature at 0.9 mm is 93.6±5.3 K (including calibration uncertainties). The observed difference of ∼3 K between all Io-in-sunlight and in-eclipse maps, together with the 22 K drop in temperature at 19 μm (Tsang et al., 2016), suggests that Io's surface is composed of a thin low-thermal-inertia (50 J m^{-2} K^{-1} $s^{-1/2}$) layer, overlying a more compact high-thermal-inertia (320 J m^{-2} K^{-1} $s^{-1/2}$) layer, indicative of a thin ($\lesssim$few mm) layer of dust or fine-grained volcanic deposits overlying more compact layers of rock and/or coarse-grained/sintered ice.

• The SO_2 and SO disk-integrated flux densities are typically about 2–3 times higher on Io-in-sunlight than in-eclipse, indicative of a 30–50% volcanic contribution to the emissions.

• During eclipse ingress, the SO_2 flux density dropped exponentially, with the 346.652 GHz transition (strongest line intensity) faster and more than the other transitions. Following eclipse egress, the SO_2 flux densities increased linearly, with the 346.652 GHz transition faster than the others.

• Eclipse egress observations show that the atmosphere is re-instated on a timescale of 10 minutes, consistent with the interpretation of the post-eclipse brightening effect reported for observations of Io's surface reflectivity. An atmospheric post-eclipse brightening was seen in several SO_2 transitions, where the flux density was up to ∼20% higher 10 min after re-emerging in sunlight compared to 1/2 hour later.

• We attribute the variations in emissions and differences between line transitions during eclipse ingress and egress, as well as the atmospheric post-eclipse brightening effect to altitude-dependent changes in temperature, likely caused in/by volcanic plumes and their interacton with the atmosphere, such as simulated by McDoniel et al. (2017).

• The SO flux density dropped/increased linearly after entering/re-emerging from eclipse, in both cases clearly delayed compared to SO_2. This provides confirmation that SO may be rapidly removed through reactions with Io's surface once in eclipse, and that photolysis of SO_2 is a major source of SO.

• Spectral image data cubes reveal bright volcanic plumes on 20 March and 2 September; no plumes were detected on 11 September. Plumes on the limb create high-velocity wings in the disk-integrated line profiles (at $\gtrsim$600 kHz, or $\gtrsim$500 m/s). Such high velocities match those predicted in plume simulations by Zhang et al. (2003) and McDoniel et al. (2017).

• In addition to the few obvious volcanic plumes in our spectral image data-cubes, the low level SO_2 emissions present during eclipse may be sourced by stealth volcanic plumes or be evidence of a layer of non-condensible gases preventing complete collapse of SO_2, as modeled by Moore et al. (2009).

• Based upon hydrostatic model calculations, typical disk-integrated SO_2 column densities and temperatures are $N_t \approx (1.5 \pm 0.3) \times 10^{16}$ cm^{-2} and $T_t \approx 220 - 320$ K both for Io-in-sunlight and in-eclipse. SO column densities are roughly a factor of 5–10 lower. The main differences between in-sunlight and in-eclipse flux densities appear to be caused by a factor of 2–3 smaller fractional coverage in-eclipse (i.e., down from 30–35% SO_2 and ∼12% SO in-sunlight).

• The active volcanoes on 20 March and 2 September show similar SO_2 column densities and temperatures as for the disk-integrated profiles, but with a very high fractional coverage (∼50–60% in sunlight, vs 30-35% disk-averaged). This seems consistent with McDoniel et al.'s (2017) simulations, where the column densities blend into the background at distances over a few 100 km from the volcanic vent.

• Line profiles of in-eclipse data are very asymmetric, both for disk-integrated profiles and individual volcanoes. Some volcanoes show red-shifted, and others blue-shifted shoulders both in-sunlight and in-eclipse. Sometimes the entire profile is slightly red- or blue-shifted. The line profiles must be strongly affected by intrinsic properties of volcanic plumes (e.g., ejection speed, direction, density, and variations therein), in addition to their viewing geometry.

• The data are suggestive of a 300–400 m/s horizontal prograde wind on 11 September, when no volcanic activity was reported; however such a wind is not supported by disk-integrated line profiles. No zonal winds were detected on 20 March and 2 September, when volcanic plumes were seen.

• KCl gas has only been detected on 20 March, sourced mainly from near Ulgen Patera. No SO or SO_2 gas was detected at this location. Hence the magma in the chambers that power volcanoes must have different melt compositions, and/or the magma has access to different surface/subsurface volatile reservoirs.

• Our data can be qualitatively explained by the night-side plume simulations of Zhang et al. (2003) and day-side simulations by McDoniel et al. (2017), although it is also clear that the data are much more complex than the models can capture.

Our observations begin to clarify the role of volcanism in forming Io's atmosphere. However, many questions still remain, including, e.g., Io's overall atmospheric temperature profile, in particular in the first 10-20 km above the surface; longitudinal variations in column density; winds; volcanic sources; magma composition. Although it is clear that low-level emissions are present during eclipse, we do not yet understand the cause of these: perhaps stealth volcanism, or a layer of non-condensible gases preventing complete collapse of the SO_2 atmosphere. To further address these questions we plan to obtain ALMA data at a higher spatial resolution when the satellite is at eastern and western elongation. Future work will also need to include realistic plume models in addition to the hydrostatic models employed here.

ACKNOWLEDGEMENTS

We are grateful for in-depth reviews by David Goldstein and one anonymous referee, which helped improve the manuscript substantially. This paper makes use of ALMA data ADS/JAO.ALMA#2017.1.00670.S. ALMA is a partnership of ESO (representing its member states), NSF (USA) and NINS (Japan), together with NRC (Canada), MOST and ASIAA (Taiwan), and KASI (Republic of Korea), in cooperation with the Republic of Chile. The Joint ALMA Observatory is operated by ESO, AUI/NRAO, and NAOJ. The National Radio Astronomy Observatory is a facility of the National Science Foundation operated under cooperative agreement by Associated Universities, Inc. The data can be downloaded from the ALMA Archive. This research was supported by the National Science Foundation, NSF grant AST-1313485 to UC Berkeley. PMR acknowledges support from ANID basal AFB170002

7. REFERENCES

Ballester, G. E., M. A. McGrath, D. F. Stobel, X. Zhu, P. D. Feldman, and H. W. Moos, Detection of the SO_2 atmosphere on Io with the Hubble Space Telescope, Icarus 111, 2-17, 1994.

Bellucci, G., Aversa, E.D., Formisano, V., et al., 2004. Cassini/VIMS observation of an Io post-eclipse brightening event. Icarus, 172, 141-148.

Binder, A.P., Cruikshank, D.P., 1964. Evidence for an atmosphere on Io. Icarus 3, 299-305.

Cornwell, T. J., and E. B. Fomalont 1999. Self-calibration. In Synthesis Imaging in Radio Astronomy II (G. B. Taylor, C. L. Carilli, and R. A. Perley, Eds.), pp. 187-199, ASP Conf. Series. Astron. Soc. of the Pacific, San Francisco.

Cruikshank, D.P., Emery, J.P., Korney, K.A., Bellucci, G., Aversa, E., 2010. Eclipse reappearances of Io: Time resolved spectroscopy (1.9–4.2 μm). Icarus, 205, 516-527.

de Kleer, K., I. de Pater, 2016. Time Variability of Io's Volcanic Activity from Near-IR Adaptive Optics Observations on 100 Nights in 2013-2015. Icarus, 280, 378-404.

de Kleer, K., de Pater, I., Molter, E., Banks, E, Davies, A., Alvarez, C., Campbell, R., et al., 2019. Io's volcanic activity from Time-domain Adaptive Optics Observations: 2013–2018. Astron. J., 158, 129 (14pp). https://doi.org/10.3847/1538-3881/ab2380

de Kleer, K., Butler, B., de Pater, I., Gurwell, M., Moullet, A., Trumbo, S., Spencer, J., 2020. Thermal properties of Ganymedes surface from millimeter and infrared emission. PSJ ??, in prep.

de Pater, I., H.G. Roe, J.R. Graham, D.F. Strobel, and P. Bernath, 2002. Detection of the Forbidden SO $a^1\Delta \rightarrow X^3\Sigma^-$ Rovibronic Transition on Io at 1.7 μm. *Icarus Note* **156**, 296-301.

de Pater, I., F. Marchis, B.A. Macintosh, H.G. Roe, D. Le Mignant, J.R. Graham, and A.G. Davies, 2004. Keck AO observations of Io in and out of eclipse. Icarus, 169, 250-263.

de Pater, I., C. Laver, F. Marchis, H.G. Roe, and B.A. Macintosh, 2007. Spatially Resolved Observations of the Forbidden SO $a^1\Delta \rightarrow X^3\Sigma^-$ Rovibronic Transition on Io during an Eclipse. Icarus, 191, 172-182.

de Pater, I., Sault, R.J., Moeckel, C., Moullet, A., Wong, M.H., Goullaud,C., DeBoer,D., Butler, B., Bjoraker, B., Ádámkovics, M., Cosentino, R., Donnelly, P.T., Fletcher, L.N., Kasaba, Y., Orton, G., Rogers, J., Sinclair, J., Villard, E., 2019. First ALMA millimeter wavelength maps of Jupiter, with a multi-wavelength study of convection. *Astron. J.*, **158**, 139 (17 pp). https://doi.org/10.3847/1538-3881/ab3643

de Pater, I., de Kleer, K., Ádámkovics, M., 2020. High Spatial and Spectral Resolution Observations of the Forbidden 1.707 μm Rovibronic SO Emissions on Io. *Planetary Science Journal*, submitted.

Fanale, F.P., Banerdt, W.B., Cruikshank, D.P., 1981. IO: Could SO_2 condensation/sublimation cause the sometimes reported post-eclipse brightening? GRL, 8, 625-628.

Feaga, L.M., McGrath, M., Feldman, P.D., 2009. Io's dayside SO_2 atmosphere. Icarus 201, 570-584.

Geissler, P.E., McEwen, A.S., Keszthelyi, L., Lopes-Gautier, R., Granahan, J., Simonelli, P., 1999. Global color variations on Io, Icarus, 140, 265-282.

Geissler, P.E., Smyth, W.H., McEwen, A.S., et al., 2001. Morphology and time variability of Io's visible aurora. J. Geophys. Res., 106, 26,137-26,146.

Geissler, P.E., McEwen, A.S., Philips, C., Keszthelyi, L., Spencer, J., 2004. Surface changes on Io during the Galileo mission. Icarus, 169, 29-64.

Geissler, P., McEwen, A., Porco, C., Strobel, D., Saur, J., Ajello, J., West, R. 2004. Cassini observations of Io's visible aurorae. Icarus, 172, 127-140.

Gratiy, S.L., Walker, A.C., Levin, D.A., Goldstein, D.B., Verghese, P.L., Trafton, L.M., Moore, C.H., 2010. Multi-wavelength simulations of atmospheric radiation from Io with a 3-D spherical-shell backward Monte Carlo radiative transfer model. Icarus, 207, 394-408.

Hammel, H.B., Goguen, J.D., Sinton, W.M., Cruikshank, D.P., 1985. Observational Tests for Sulfur AI-Iotropes on Io. Icarus, 64, 125-132.

Hapke, B., Graham, F., 1989. Spectral properties of condensed phases of disulfur monoxide, polysulfur oxide, and irradiated sulfur. Icarus, 79, 4755.

Ingersoll, A.P., Summers, M.E., Schlipf, S.G., 1985. Supersonic meteorology of Io: Sublimation-driven flow of SO_2. Icarus 64, 375-390.

Jessup, K.L., Spencer, J.R., Yelle, R., 2007. Sulfur volcanism on Io. Icarus 192, 24-40.

Johnson, T. V., Matson, D. L., Blaney, D.L., Veeder, G.J., Davies, A., 1995. Stealth plumes on Io, Geophys. Res. Lett. 22, 3293-3296.

Kieffer, S.W., Lopes-Gautier, R., McEwen, A., Smythe, W., Keszthelyi, L., Carlson, R., 2000. Prometheus: Io's wandering plume. Science 288, 1204 -1208.

Kumar, S. 1985. The SO_2 atmosphere and ionosphere of Io: Ion chemistry, atmospheric escape, and models corresponding to the Pioneer 10 radio occultation measurements. Icarus, 61, 101-123.

Lellouch, E., M.J.S. Belton, I. de Pater, S. Gulkis, and T. Encrenaz, 1990, Io's atmosphere from microwave detection of SO_2, Nature, 346, 639-641.

Lellouch, E., M. Belton, I. de Pater, G. Paubert, S. Gulkis, and Th. Encrenaz, 1992, The Structure, Stability, and Global Distribution of Io's Atmosphere, Icarus, 98, 271-295.

Lellouch, E., 1996. Urey Prize Lecture. Io's Atmosphere: Not Yet Understood. Icarus, 124, 1-21.

Lellouch, E., Paubert, G., Moses, J. I., Schneider, N. M., and Strobel, D. F., 2003. Volcanically-emitted sodium chloride as a source for Io's neutral clouds and plasma torus. Nature 421, 45-47.

Lellouch, E., Strobel, D. Belton, M., Paubert, G., Ballester, G., de Pater, I., 1994, Millimeter wave obervations of Io's atmosphere: new data and new models, BAAS, 26, 1136.

Lellouch, E., Paubert, G., Moses, J. I., Schneider, N. M., and Strobel, D. F. 2003. Volcanically-emitted sodium chloride as a source for Io's neutral clouds and plasma torus. Nature, 421, 45-47.

Lellouch, E., McGrath, M. A., Jessup, K. L., 2007. Io's atmosphere, in *Io after Galileo: A New View of Jupiter's Volcanic Moon*. Eds. Lopes, R.M., & Spencer, J. R. Springer. ISBN 3-540-34681-3.

Lellouch, E., Ali-Dib, M., Jessup, K.-L., Smette, A., Käufl, H.-U., Marchis, F., 2015. Detection and characterization of Io's atmosphere from high-resolution 4-μm spectroscopy. Icarus, 253, 99-114.

Macintosh, B., D. Gavel, S.G. Gibbard, C.E. Max, I. de Pater, A. Ghez, and J. Spencer. 2003. Speckle imaging of volcanic hot spots on Io with the Keck telescope. Icarus, 165, 137-143.

Marchis, F., D. Le Mignant, F. Chaffee, A.G. Davies, T. Fusco, R. Pranage, I. de Pater and the Keck Science team, 2005. Keck AO survey of Io's global volcanic activity between 2 and 5μm. Icarus, 176, 96-122.

McDoniel, W.J., Goldstein, D.B., Varghese, P.L., and Trafton, L.M., 2017. The interaction of Io's plumes and sublimation atmosphere. Icarus, 294, 81-97.

McEwen, A.S., Soderblom, L.A., 1983. Two classes of volcanic plumes on Io. Icarus 58, 197-226.

McGrath, M.A., Lellouch, E., Strobel, D.F., Feldman, P.D., Johnson, R.E., 2004. Satellite atmospheres. In *Jupiter: Planet, Satellites & Magnetosphere*, Eds. F. Bagenal, T. E. Dowling, and W. McKinnon, pp. 457-483. Cambridge, UK: Cambridge University Press.

McGrath, M.A., Belton, M.J.S., Spencer, J.R., Sartoretti, P., 2000. Spatially resolved spectroscopy of Io's Pele plume and SO_2 atmosphere. Icarus 146, 476-493.

Moore, C., Goldstein, D. B., Varghese, P., Trafton, L. and Stewart, B. 2009. 1-D DSMC simulation of Io's atmospheric collapse in eclipse. Icarus, 201, 585-597.

Morrison, D., Cruikshank, D. P. 1973. Thermal properties of the Galilean satellites. Icarus, 18, 224-236.

Moses, J. I., Nash, D.B., 1991. Phase transformations and the spectral reflectance of solid sulfur - Can metastable sulfur allotropes exist on Io?, Icarus 89, 277-304.

Moses, J.I., Zolotov, M.Y., Fegley, B. Jr., 2002. Photochemistry of a volcanically driven atmosphere on Io: Sulfur and oxygen species from a Pele-type eruption. Icarus, 156, 76-106.

Moullet, A., Lellouch, E., Moreno, R., Gurwell, M.A., Moore, C., 2008. First disk- resolved millimeter observations of Io's surface and SO_2 atmosphere. Astrophys. Astron. 482, 279-292. doi:10.1051/0004-6361:20078699.

Moullet, A., Gurwell, M.A., Lellouch, E., Moreno, R., 2010. Simultaneous mapping of SO_2, SO, NaCl in Io's atmosphere with the Submillimeter Array. Icarus, 208, 353-365.

Moullet, A. et al., 2013. Exploring Ios atmospheric composition with APEX: First measurement of 34SO2 and tentative detection of KCl. Astrophys. J. 776, 32. http://dx.doi.org/10.1088/0004-637X/776/1/32, 9 pp.

Moullet, A., 2015. Exploring the Solar System with ALMA. 2015. *Revolution in Astronomy with ALMA: The third year.* ASP Conference Series, Vol. 499. Daisuke Iono, Ken'ichi Tatematsu, Al Wootten, Leonardo Testi, eds. Astronomical Society of the Pacific

Moullet, A, Lellouch, E, Gurwell, M, Moreno, R, Black, J, Butler, B. 2015. AAS DPS Meeting #47, Abstract 311.31

Nicholson, P. D., P. J. Gierasch, T. L. Hayward, C. A. McGhee, J. E. Moersch, S. W. Squyres, J. Van Cleve, K. Matthews, G. Neugebauer, D. Shupe, A. Weinberger, J. W. Miles, and B. J. Conrath, 1995. Palomar observations of the R impact of comet Shoemaker-Levy 9: I. Light curves, Geophys. Res. Lett. 22, 16131616.

Pearl, J., Hanel, R., Kunde, V., Maguire, W., Fox, K., Gupta, S., Ponnamperuma, C., Raulin, F., 1979. Identification of gaseous SO_2 and new upper limits for other gases on Io. Nature 280, 755-758. doi:10.1038/280755a0.

Rathbun, J.A., Spencer, J.R., Tamppari, L.K., Martin, T.Z., Barnard, L., Travis, L.D., 2004. Mapping of Io's thermal radiation by the Galileo photopolarimeter-radiometer (PPR) instrument. Icarus, 169, 127-139.

Retherford, K.D., Spencer, J.R., Stern, S.A., et al., 2007. Io's atmospheric response to eclipse: UV aurorae observations. Science 318, 237-241.

Roesler, F.L., Moos, H.W., Oliversen, R.J., Woodward, R.C., Retherford, K.D., Scherb, F., McGrath, M.A., Smyth, W.H., Feldman, P.D.F., Stro bel, D., 1999. Far-ultraviolet imaging spectroscopy of Io's atmosphere with HST/STIS. Science 283, 353-357.

Saur, J., Strobel, D.F., 2004. Relative contributions of sublimation and volcanoes to Io's atmosphere inferred from its plasma interaction during solar eclipse. Icarus, 171, 411-420.

Schenk, P. W., Steudel, R., 1965. New findings in the chemistry of the lower oxides of sulfur. Angewandte Chem. Intern. Ed. Engl. 4, 402-409.

Sinton, W.M., Kaminsky, C., 1988. Infrared observations of eclipses of Io, its thermophysical parameters, and the thermal radiation of the Loki volcano and environs. Icarus, 75, 207-232.

Spencer, J. R., 1987. The Surfaces of Europa, Ganymede, and Callisto: An Investigation Using Voyager IRIS Thermal Infrared Spectra, Ph.D. thesis, University of Arizona.

Spencer, J.R., N.M. Schneider, 1996. Io on the eve of the Galileo mission. Ann. Rev. Earth and Plan. Sci., 24, 125-190.

Spencer, J. R., L. K. Tamppari, T. Z. Martin, and L. D. Travis, 1999. Temperatures on Europa from Galileo PPR: Nighttime thermal anomalies, Science 284, 15141516, 1999.

Spencer, J.R., Lellouch, E., Richter, M.J., López-Valverde, M.A., Lea Jessup, K., Greathouse, T.K., Flaud, J.-M., 2005. Mid-infrared detection of large longitudinal asymmetries in Io's SO_2 atmosphere. Icarus 176, 283-304.

Spencer, J.R., Stern, S.A., Cheng, A.F., et al., 2007. Io volcanism seen by New Horizons: A major eruption of the Tvashtar volcano. Science, 318, 240-243.

Strobel, D.F., Zhu, X., Summers, M.E., 1994. On the vertical structure of Io's atmosphere. Icarus 111, 18-30.

Summers, M. E. 1985. Theoretical studies of Io's atmosphere. Ph.D. thesis, California Institute of Technology, Pasadena.

Tsang, C.C.C., Spencer, J.R., Jessup, K.L., 2015. Non-detection of post-eclipse changes in Io's Jupiter-facing atmosphere: Evidence for volcanic support? Icarus, 248, 243-253.

Tsang, C.C.C., Spencer, J.R., Lellouch, E., Lopes-Valverde, M.A., Richter, J.J., 2016. The collapse of Io's primary atmosphere in Jupiter eclipse. JGR 121, 1400-1410.

Wagman, D. D. 1979. Sublimation Pressure and Enthalpy of $S0_2$. Chem. Thermodynamics Data Center, Nat. Bureau of Standards, Washington, DC.

Walker, A.C., Gratiy, S.L., Goldstein, D.B., Moore, C.H., Varghese, P.L., Trafton, L.M., Levin, D.A., Stewart, B.D., 2010. A comprehensive numerical simulation of Io's sublimation driven atmosphere. Icarus 207, 409-432.

Walker, A., Moore, C., Goldstein, D., Varghese, P., Trafton, L. 2012. A parametric study of Io's thermophysical surface parameters and subsequent numerical atmospheric simulations based on the best fit parameters. Icarus, 220, 225-253.

Zhang, J., Goldstein, D. B., Varghese, P. L., Gimelshein, N. E., Gimelshein, S. F., and Levin, D. A. 2003. Simulation of gas dynamics and radiation in volcanic plumes of Io. Icarus, 163, 182-187.

Zhang, J., Goldstein, D., Varghese, P., Trafton, L., Moore, C., Miki, K., 2004. Numerical modeling of Ionian volcanic plumes with entrained particulates. Icarus, 172 , 479-502.

Table 1: ALMA data: Species and frequencies

Species	Frequency (GHz)	wavelength mm	Line strength (cm^{-1}/mol/cm^2)	E (low) (cm^{-1})	Spectral window spw	Bandwidth total (MHz)	Channel width (kHz)
Continuum	334.100	0.897			0	2000	15625
SO_2	346.524	0.865	6.18556E-22	102.750	1	117	122
SO	346.528	0.865	5.34047e-21	43.1928	1	117	122
SO_2	346.652	0.865	1.11142E-21	105.299	2	117	122
SO	344.311	0.871	4.50069e-21	49.3181	3	117	122
KCl	344.820	0.869	2.23552e-19	253.489	4	117	122
SO_2	332.091	0.903	3.10870e-22	141.501	5	117	122
SO_2	332.505	0.902	2.65693e-22	10.6590	6	58.6	122
SO_2	333.043	0.900	2.42761e-23	643.771	7	58.6	122

All transitions are taken from https://spec.jpl.nasa.gov.

Table 2: Time table of observations in 2018

Date Start time month-day hr:m:s	End time hr:m:s	Sub-long. deg (W)	Sub-lat. deg	Scans combined	Diameter Io arcsec	Array conf.	HPBW arcsec	HPBW km	Comments
03-20 10:02:29	10:21:41	337.2	-3.40	7,11,15 in set 1	1.058	C43-4	0.35	1205	sunlight
03-20 10:54:43	11:01:18	343.7	-3.40	7 in set 2	1.058	C43-4	0.35	1205	eclipse
03-20 10:54:43	10:57:40	343.4	-3.40	7a in set 2	1.058	C43-4	0.35	1205	eclipse
03-20 10:57:40	11:01:18	343.8	-3.40	7b in set 2	1.058	C43-4	0.35	1205	eclipse
03-20 11:03:19	11:13:54	345.1	-3.40	11,15 in set 2	1.058	C43-4	0.35	1205	eclipse
09-02 21:46:21	21:53:00	19.5	-2.96	6 in set 1	0.885	C43-3	0.30	1235	(partial) eclipse
09-02 21:46:21	21:49:40	19.2	-2.96	6a in set 1	0.885	C43-3	0.30	1235	eclipse
09-02 21:49:40	21:53:00	19.7	-2.96	6b in set 1	0.885	C43-3	0.30	1235	partial eclipse
09-02 21:54:01	22:00:36	20.5	-2.96	8 in set 1	0.885	C43-3	0.30	1235	sunlight
09-02 21:54:01	21:57:20	20.3	-2.96	8a in set 1	0.885	C43-3	0.30	1235	sunlight
09-02 21:57:20	22:00:36	20.7	-2.96	8b in set 1	0.885	C43-3	0.30	1235	sunlight
09-02 22:01:22	22:04:28	21.3	-2.96	10,12 in set 1	0.885	C43-3	0.30	1235	sunlight
09-02 22:22:00	22:40:08	25.3	-2.96	6,8,10,12 in set 2	0.885	C43-3	0.30	1235	sunlight
09-11 17:36:12	17:54:03	14.8	-2.95	6,8,10,12 in set 1	0.867	C43-5	0.22	924	eclipse
09-11 18:24:01	18:41:56	21.5	-2.95	6,8,10,12 in set 2	0.867	C43-5	0.22	924	sunlight

Io's diameter is 3642 km.
Sub-long, sub-lat are Observers' sub-longitude and sub-latitude.
On each day, 2 sets of data were taken, typically one when Io was in eclipse and one when it was in sunlight.
Sans 6, 7, 8 and 11 are 6–7 min long; scans 10, 12 and 15 are typically 1-2 min long.
March 20: partial eclipse started at 10:46:40; full eclipse started at 10:50:22.
Sep. 02: partial eclipse started 21:49:45, and ended 21:53:29.
Sep. 11: partial eclipse started 18:13:52, and ended: 18:17:35. There was no difference between sunlight scans 6, 8, 10, and 12; nor between first and last half of scan 6.

Table 3: Analysis of SO_2 and SO line profiles from disk-integrated spectra

Date	species	$fr^1_{\rm map}$ %	fr^2_t %	N^2_t $\times 10^{16}$ cm^{-2}	T^2_t K	$v^2_{r,t}$ m/s	comments
03-20	SO_2	31±3	32±1	1.35±0.25	$270\pm^{+50}_{-25}$	+20±7	sunlight
03-20	SO_2	17±2	17±2	1.35±0.25	$270\pm^{+50}_{-25}$	+20±7	eclipse, scan 11+15
03-20	SO	16±3	14±1	0.1±0.03	270[3]	0	sunlight
03-20	SO	3±2	5±2	0.13±0.03	270[3]	0	eclipse, scan 11+15
09-02	SO_2	34±3	38±1	1.5±0.3	270±25	0	sunlight, set 2
09-02	SO_2	11±1	13±2	$3\pm^{+2}_{-1}$	270±50	0	eclipse, scan 6
09-02	SO	10±2	10.5±1	0.3±0.1	270[3]	−100±10	sunlight, set 2
09-02	SO	1±2	4.5±1	$0.15\pm^{0.1}_{0.05}$	270[3]	−100±10	eclipse, scan 6
09-11	SO_2	35±3	35±2	1.5±0.3	270±25	0	sunlight
09-11	SO_2	12±1	12±2	1.5±0.3	270±50	0	eclipse
09-11	SO	8±2	8±1	$0.15\pm^{+0.1}_{-0.05}$	270[3]	0	sunlight
09-11	SO	2±2	–	–	–	–	eclipse

[1]: Fractional coverage $fr_{\rm map}$ as determined from the spw2 maps for SO_2, and spw1 maps for SO.
[2]: Fractional coverage fr_t, Column density N_t, temperature T_t, and radial velocity $v_{r,t}$ for the global (disk-integrated) atmosphere.
[3]: We set the temperature equal to that determined from the SO_2 line profiles.

Table 4: Analysis of SO_2 line profiles for individual volcanoes

Date	Volcano	fr^1_v %	N^1_v $\times 10^{16}$ cm^{-2}	T^1_v K	$v^1_{r,v}$ m/s	comments
03-20	Karei P.	48±2	1.2±0.3	270±40	+60±7	Sunlight
03-20	Karei P.	15±2	2±0.5	270±50	+60±10	eclipse, scan 11+15
03-20	Daedalus P.	46±1	1.5±0.2	$220\pm^{+50}_{-25}$	−40±7	Sunlight
03-20	Daedalus P.	40±10	1.5±1	$170\pm^{+50}_{-25}$	−40±20	eclipse, scan 11+15
09-02	P207	61±1	1.2±0.2	220±25	0	sunlight, set 2
09-02	P207	25±10	2±1	250±50	0	eclipse, scan 6
09-02	Nyambe P.	55±10	1±0.3	270±50	0	sunlight, set 2
09-02	Nyambe P.	20±5	1±0.3	270±50	0	eclipse, scan 6

[1]: Column density N_v, temperature T_v, fractional coverage fr_v, and radial velocity $v_{r,v}$ for individual volcanoes. However, note that the models are hydrostatic models, i.e., not particularly well suited for active volcanoes.

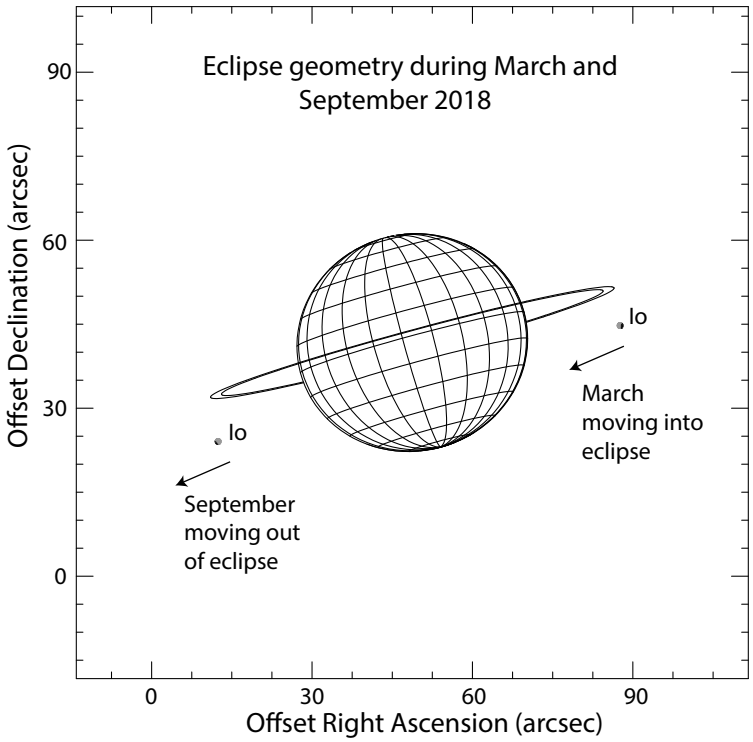


Figure 1. The geometries of Io moving into eclipse (March 2018) and coming out of eclipse (September 2018). (Adapted from the Planetary Ring Node: http://pds-rings.seti.org/tools/).

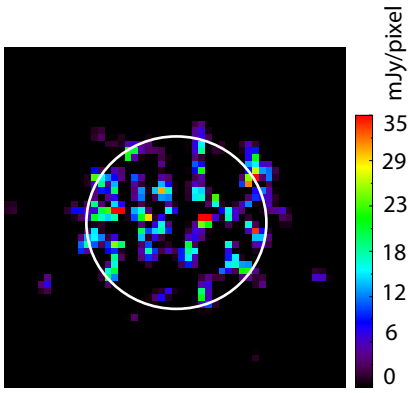


Figure 2. This .model map shows the sum of all CLEAN components per pixel as obtained from CASA's tCLEAN routine when deconvolving the original Io-in-sunlight map at 346.652 GHz. After convolution with the HPBW, and restoration to the residual map, this particular .model map results in the map displayed in the top left panel of Fig. 4.

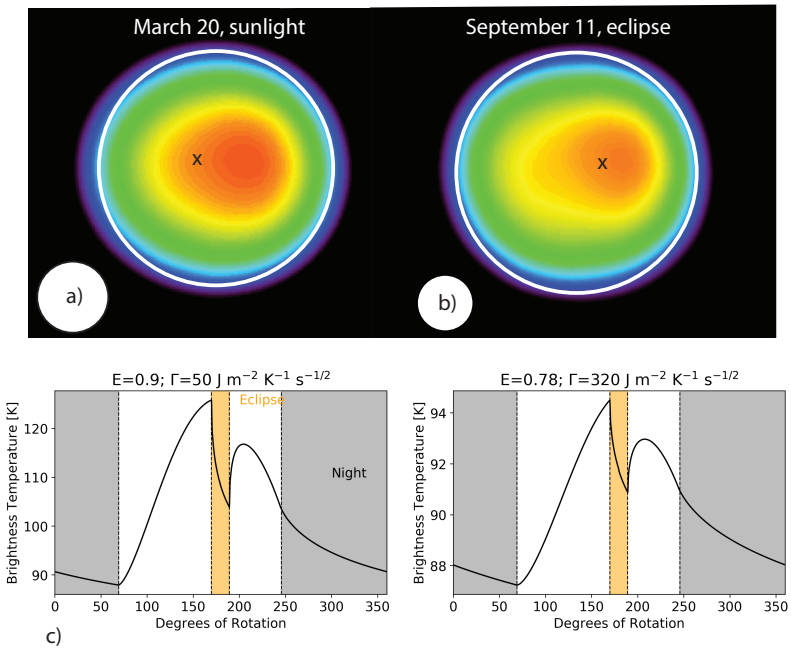


Figure 3. Continuum image of Io at 334.1 GHz taken on 20 March 2018 while Io was in sunlight (panel a), and on 11 September while Io was in eclipse (panel b). Io North is up in these images. The white circle shows the approximate size of Io's disk. The X indicates the approximate sub-solar location, and the approximate beam size is indicated in the lower left corner. The temperature scale is from 0 to ∼90 K, but not quite linear to bring out the slight asymmetry in the emission. c) Simple thermal conduction model at mid-latitudes that can explain the differences in brightness temperature between the infrared and millimeter data when entering an eclipse. (see text for details).

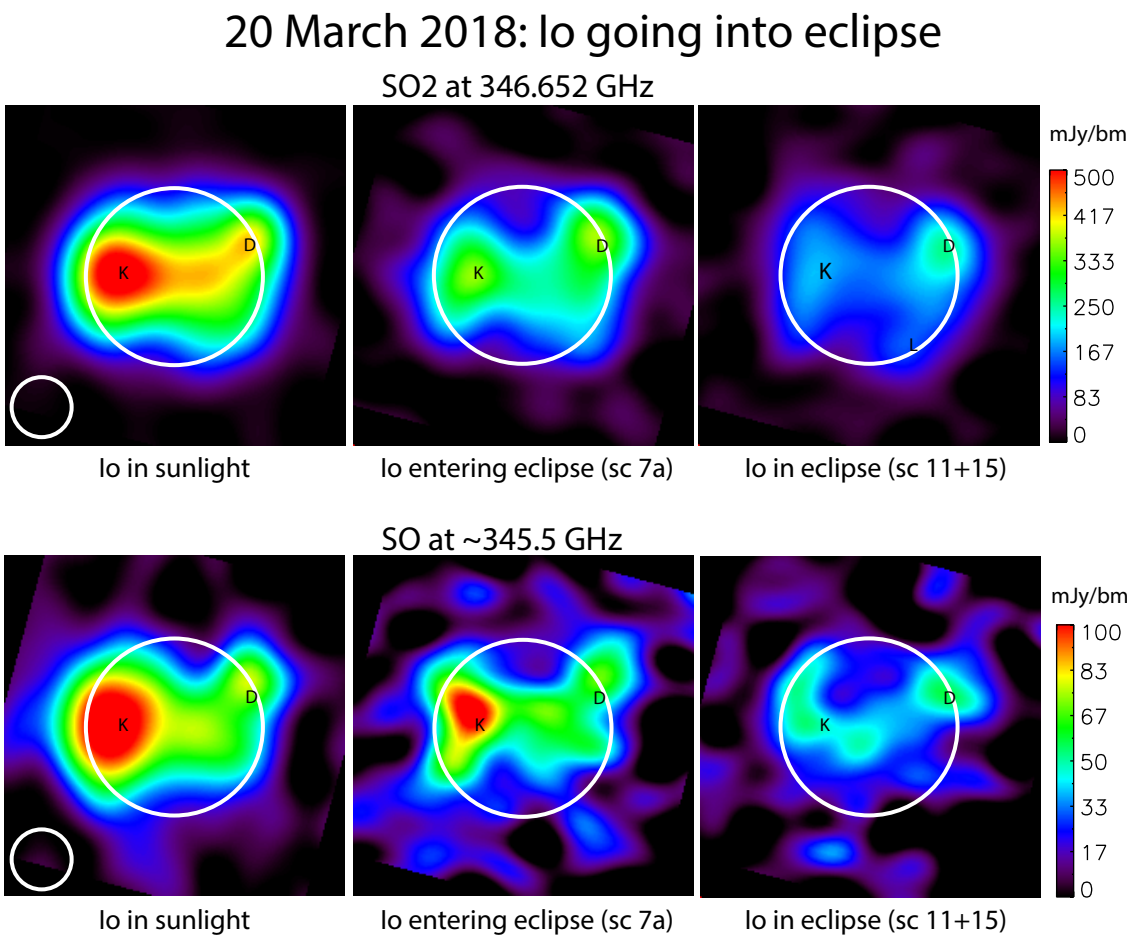


Figure 4. Top row: Maps of the spw2 data of the SO_2 distribution on Io-in-sunlight, and ~ 6 (scan 7a) and ~ 15 (scans 11+15) min after entering eclipse. Bottom row: maps of the averaged spw1 & spw3 SO data taken at the same times as the SO_2 maps. All maps were averaged over 0.4km/s ($\sim$0.45 MHz). Io North is up in all frames. The large circle shows the outline of Io, and the small circle in the lower left shows the size of the beam (HPBW). The volcanoes Karei Patera (K), Daedalus Patera (D), and North Lerna (L, on one panel only) are indicated.

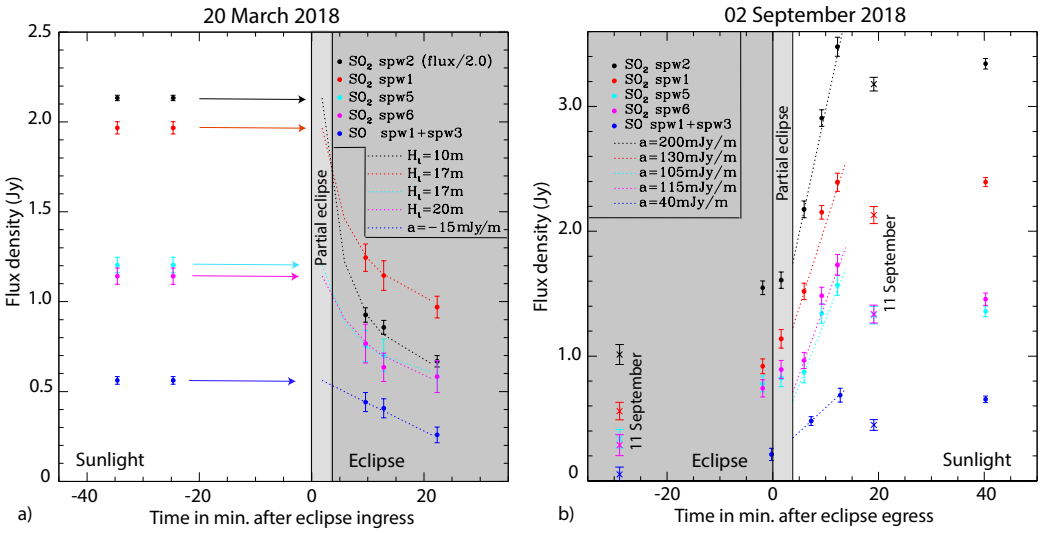


Figure 5. Flux densities integrated over individual maps (as in Figs. 4, 6, and 7) as a function of time (filled circles for March 20 and September 2 ; crosses (x) for Sep. 11). The colors refer to different spectral windows. The data for SO were averaged over spw1 and spw3 to increase the SNR. The dotted lines superposed on the data in panel a show the exponential decrease (equ. 1) or the linear slope (equ. 2) after entering eclipse, whichever is appropriate. In panel b the dotted lines show the linear increase after emerging from eclipse on September 2. All data are normalized to a geocentric distance of 5.044 AU.

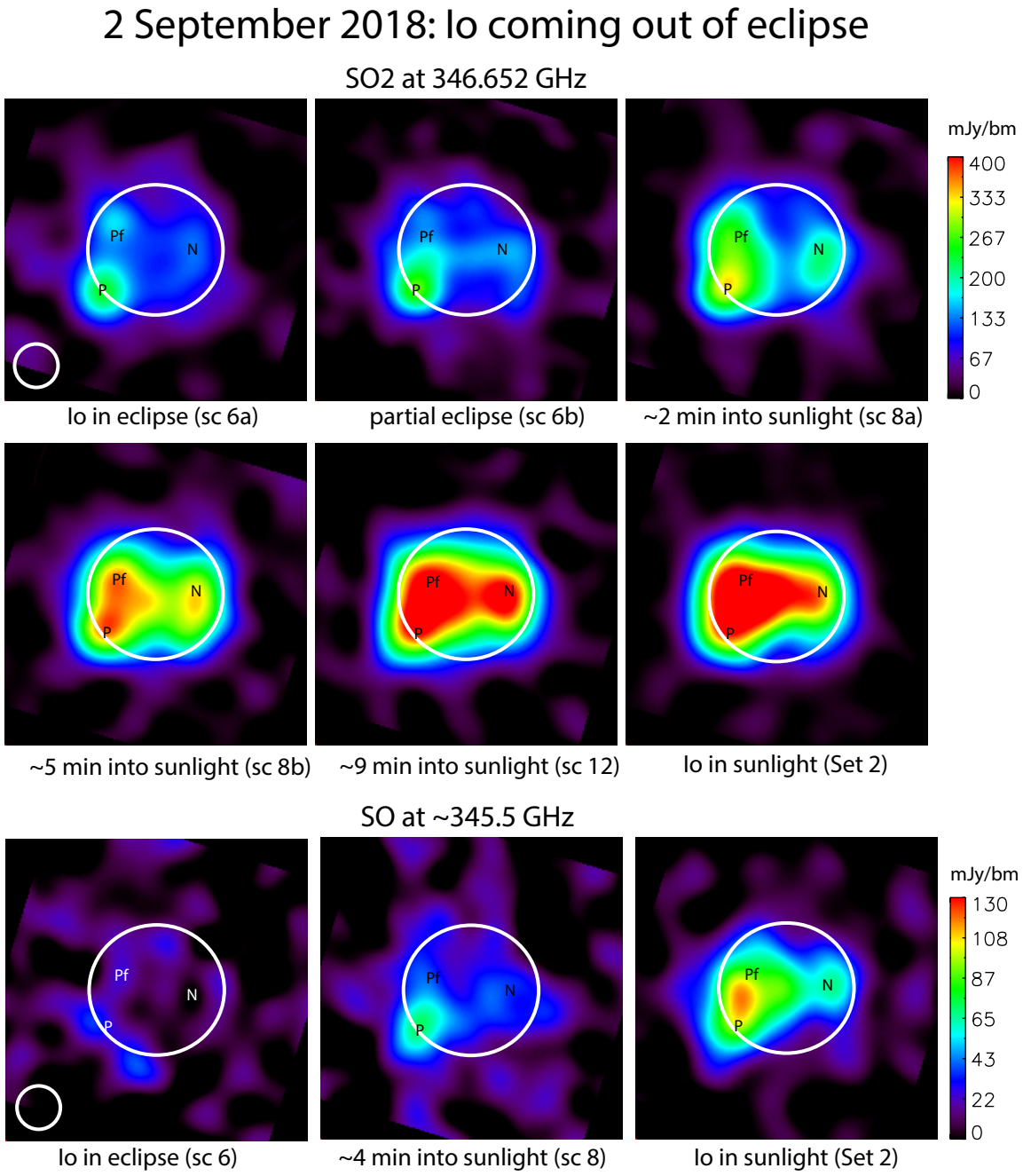


Figure 6. Top 2 rows: Maps of the spw2 data of the SO_2 distribution on Io in eclipse (scan 6a), and emerging into sunlight on 2 Sep. 2018, starting with a partial eclipse (scan 6b), as indicated. Bottom row: maps of the averaged spw1 & spw3 SO data. All maps were averaged over 0.4km/s (~0.45 MHz). See Table 2 for exact times of each scan. Io North is up. The large circle shows the outline of Io. The small circle in the lower left shows the HPBW. The letters show the positions of several volcanoes: P for P207; Pf for PFd1691, and N for Nyambe Patera.

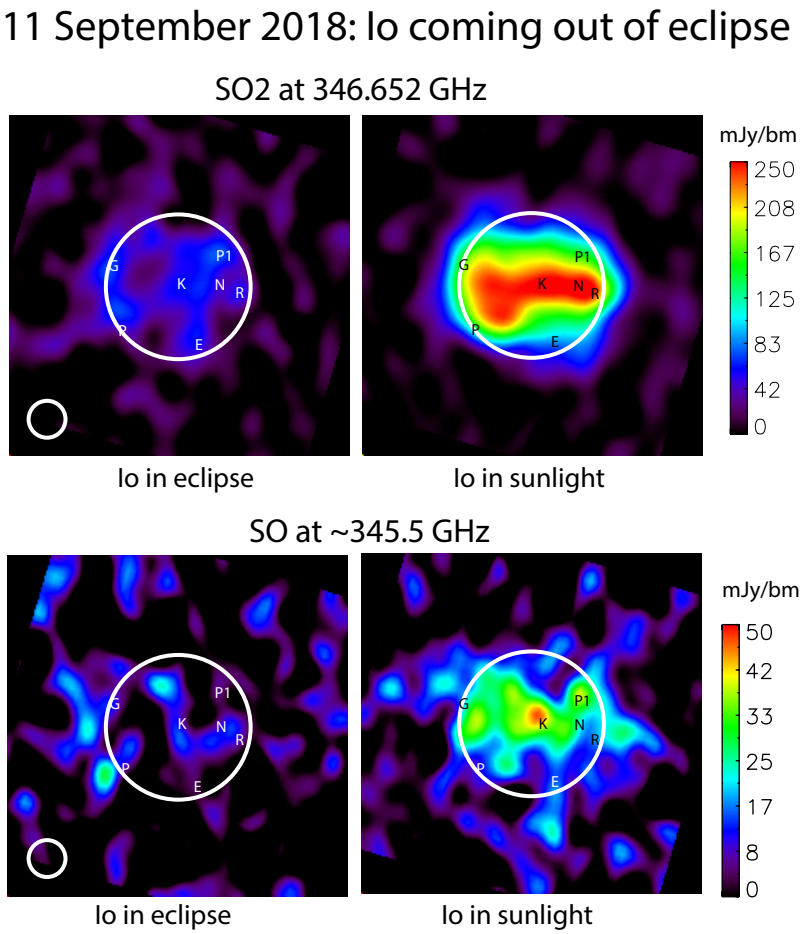


Figure 7. Top row: Maps of the spw2 data of the SO_2 distribution on Io in eclipse and in sunlight on 11 Sep. 2018. Bottom row: Maps of the SO distribution on Io in sunlight, and in eclipse on 11 Sep. 2018. The maps from spw1 and spw3 were averaged to increase the SNR. Io North is up in these frames. All maps were averaged over 0.4km/s (∼0.45 MHz). The large circle shows the outline of Io. The small circle in the lower left shows the HPBW. Note that the beam is smaller than in figures 6 and 4, so that the intensity scale on the right shows values that are much smaller than in the other figures. The letters show the positions of several volcanoes: P: P207; G: Gish Bar Patera; K: Karei Patera; N: Nyambe Patera; P1: P129; R: Ra Patera, E: Euboea.

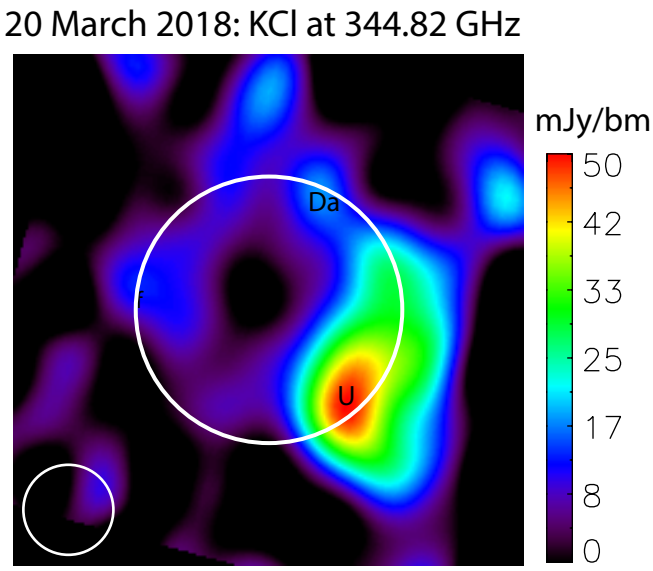


Figure 8. Map of the spatial distribution of KCl on 20 March 2018. The map was averaged over 0.4km/s (∼0.45 MHz). Io North is up in this frame. This map is from the sunlight data only, and is essentially the same as one in which sunlight and eclipse data are averaged. The volcanoes indicated on this map are: U: Ulgen Patera; Da: Dazhbog Patera.

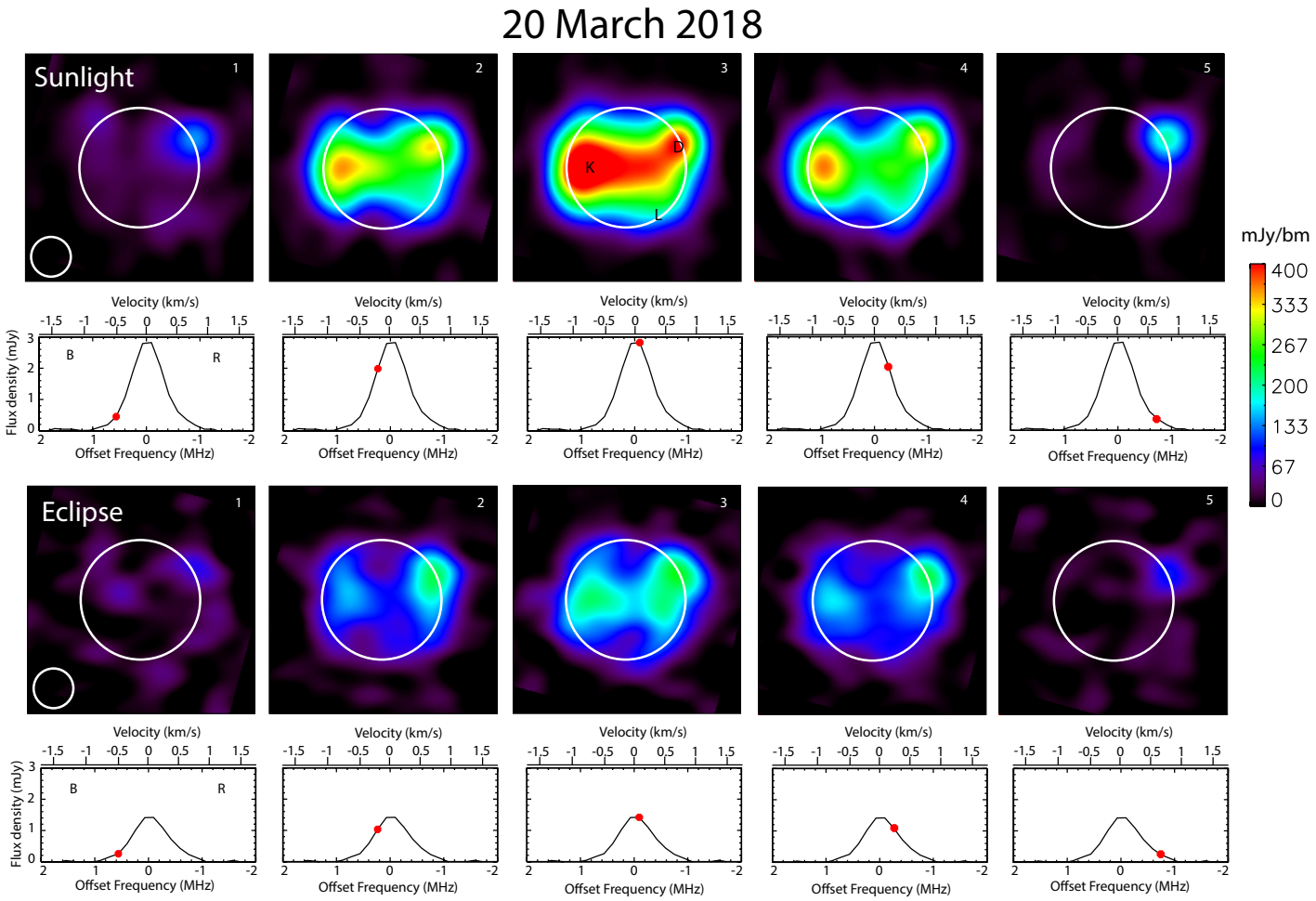


Figure 9. Individual frames at a few different frequencies (or velocities) from our March sunlight → eclipse data for the combined SO_2 spw1 & spw2 data. All scans 7–15 were averaged for the in-eclipse (Set 2; Table 2) and separately for the in-sunlight data. Each frame is averaged over 0.142 km/s or ∼ 0.16 MHz, and the line is centered on Io's frame of reference. Below each frame we show the line profile for the disk-integrated flux density as a function of offset frequency (from +2 to –2 MHz), with an approximate velocity scale at the top. The red dot on the line profile indicates the frequency of the map above. The symbols B and R stand for blueshift and redshift, resp., i.e., gas moving towards (B) or away from us (R). Note that, just due to the rotation of Io, the west limb (left side of Io) moves towards us, and the east limb away from us. The approximate positions of several volcanoes are indicated on frame 3 in-sunlight (see Fig. 4 for the symbols). Io North is up in these frames. An animation of this figure is available. The video shows a 14 image sequence in sunlight (left) and in eclipse (right). The duration of the video is 7 seconds.

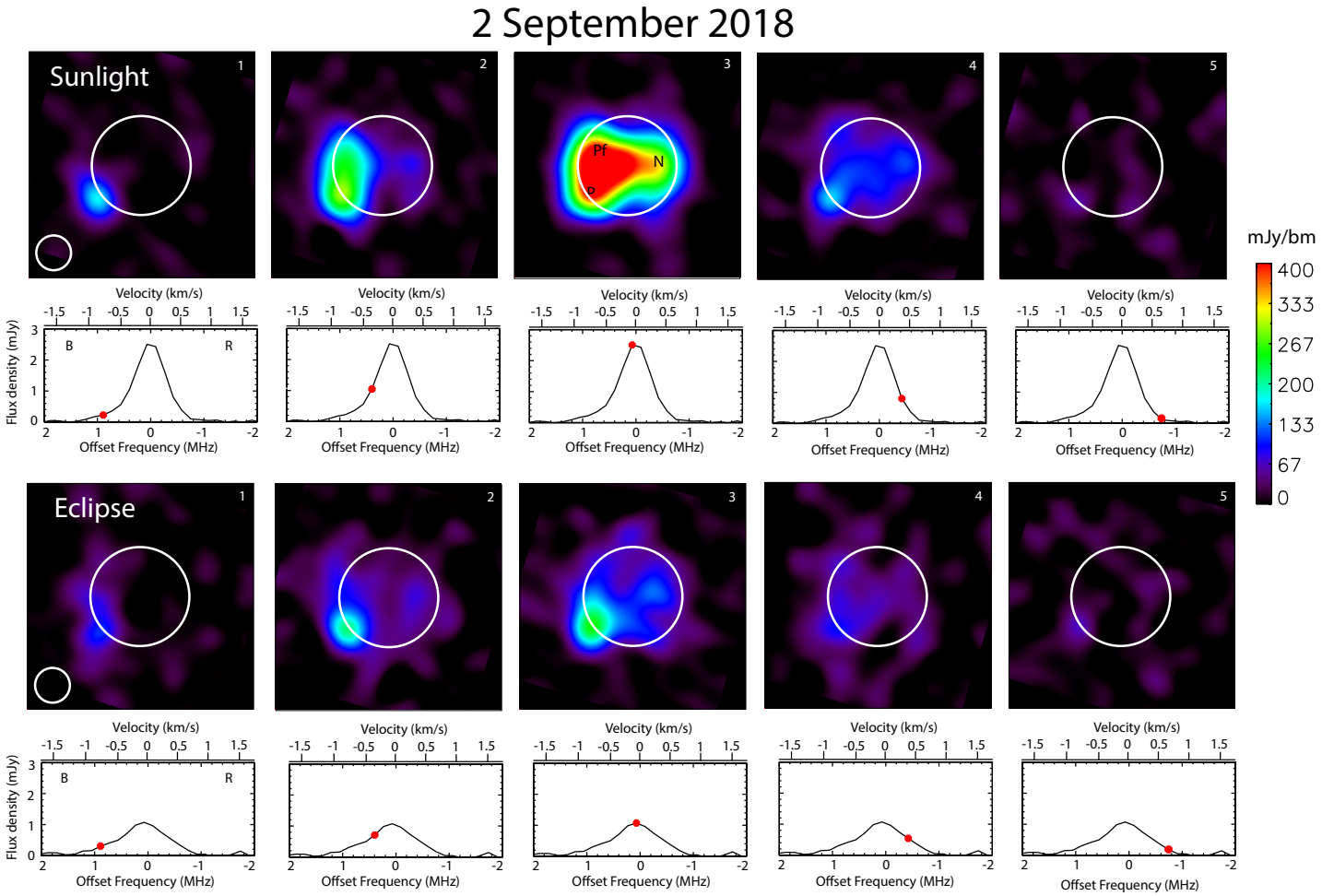


Figure 10. Individual frames at a few different frequencies (or velocities) from our 2 September eclipse → sunlight data for the combined SO_2 spw1 & spw2 data. For the eclipse data we show results for scan 6 only (6a+6b); the sunlight scans are for set 2 (see Table 2). Each frame is averaged over 0.142 km/s or ∼ 0.16 MHz, and the line is centered on Io's frame of reference. Below each frame we show the line profile for the disk-integrated flux density as a function of offset frequency (from +2 to −2 MHz), with an approximate velocity scale at the top. The red dot indicates the frequency of the map above. The symbols B and R stand for blueshift and redshift, resp., i.e., gas moving towards (B) or away from us (R). Note that, just due to the rotation of Io, the west limb (left side of Io) moves towards us, and the east limb away from us. The approximate positions of several volcanoes are indicated on frame 3 in-sunlight (see Fig. 6 for the symbols). Io North is up in these frames. An animation of this figure is available. The video shows a 16 image sequence in sunlight (left) and in eclipse (right). The duration of the video is 8 seconds.

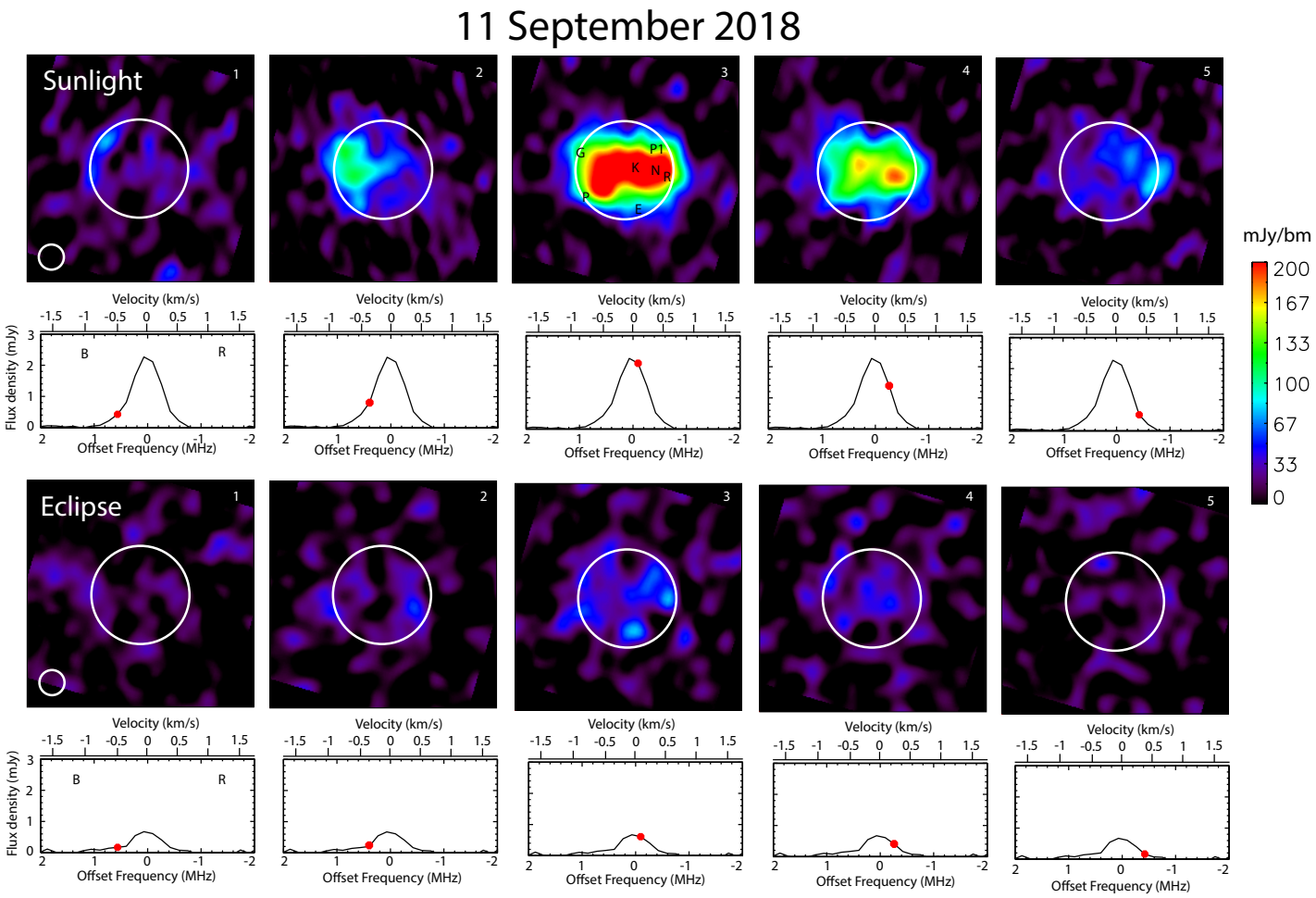


Figure 11. Individual frames at a few different frequencies (or velocities) from our 11 September eclipse → sunlight data for the combined SO_2 spw1 and spw2 data. Each frame is averaged over 0.142 km/s or ∼ 0.16 MHz, and the line is centered on Io's frame of reference. Below each frame we show the line profile for the disk-integrated flux density as a function of offset frequency (from +2 to –2 MHz), with an approximate velocity scale at the top. The red dot indicates the frequency of the map above. The symbols B and R stand for blueshift and redshift, resp., i.e., gas moving towards (B) or away from us (R). Note that, just due to the rotation of Io, the west limb (left side of Io) moves towards us, and the east limb away from us. The approximate positions of several volcanoes are indicated on frame 3 in-sunlight (see Fig. 7 for the symbols). Io North is up in these frames. An animation of this figure is available. The video shows a 11 image sequence in sunlight (left) and in eclipse (right). The duration of the video is 6 seconds.

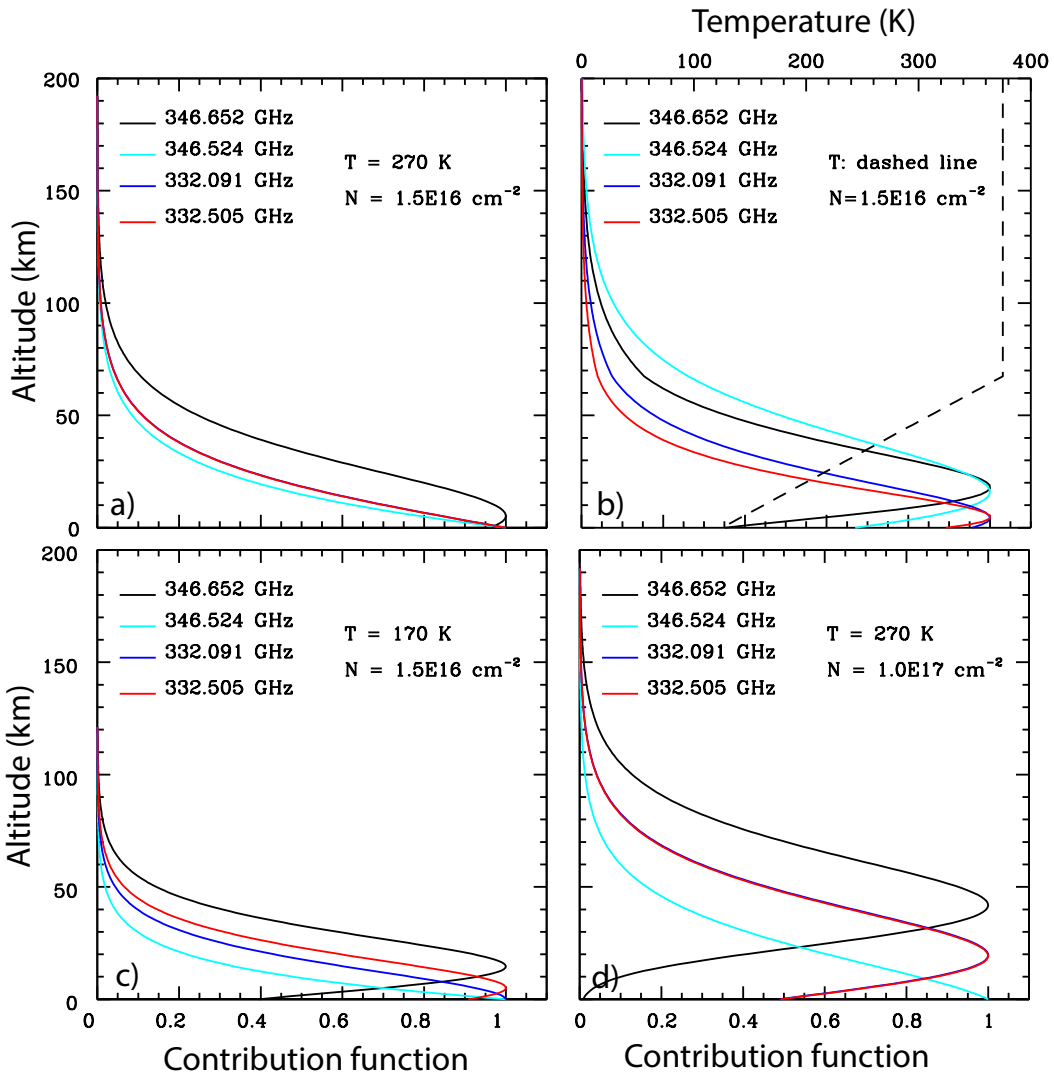


Figure 12. Sample disk-averaged contribution functions for the four SO_2 transitions detected in our ALMA data, based upon our uniform, hydrostatic model atmosphere. a) Contribution functions for a column density ($N_t = 1.5 \times 10^{16}$ cm^{-2}) and isothermal temperature ($T = 270$ K) that match most of our data (Sections 4.3, 4.4). b) A temperature profiles as indicated by the dashed line. This profile is inspired by profiles affected by plasma heating from above, such as shown by Gratiy et al. (2010). Resulting line profiles do *not* match our data. c) Contribution functions from panel a for a much colder isothermal atmosphere ($T = 170$ K). Resulting line profiles do *not* match our data. d) Contribution functions from panel a for a much higher column abundance ($N_t = 10^{17}$ cm^{-2}), such as expected on the anti-jovian hemisphere. Resulting line profiles do *not* match our data.

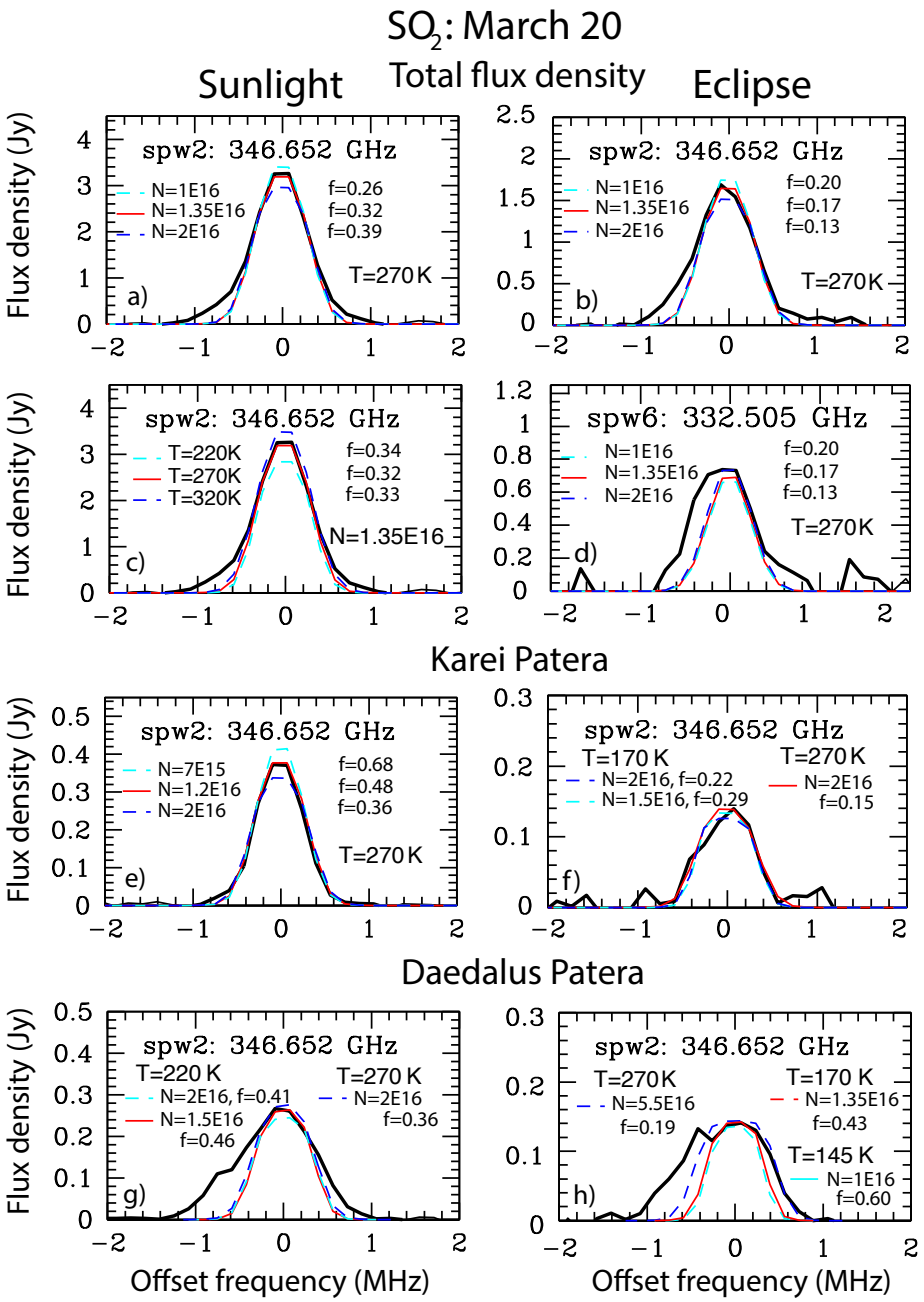


Figure 13. SO_2 line profiles (in black) with superposed various models. The red lines show the best fit models. All panels show data and models at 346.652 GHz (spw2), except for panel d. a) Disk-integrated flux density for Io-in-sunlight, with superposed the best fit ($N_t = 1.35 \times 10^{16}$ cm^{-2}) model at the best fit temperature $T_t = 270$ K, and a fractional coverage $fr_t = 0.32$ (in red). Several models are shown to provide a sense on the accuracy of the numbers; the fractional coverage for these models is indicated on the right side of the line profile. b) Disk-integrated flux density for Io-in-eclipse, with superposed the best fit ($N_t = 1.35 \times 10^{16}$ cm^{-2}), $T_t = 270$ K, $fr_t = 0.17$ (in red). c) Same as panel a to show the sensitivity on the temperature. d) Same as panel b, but at 332.505 GHz (spw6). e–h): data for Karei and Deadalus Paterae, integrated over 1 beam diameter (in black). Various hydrostatic models are superposed, as indicated.

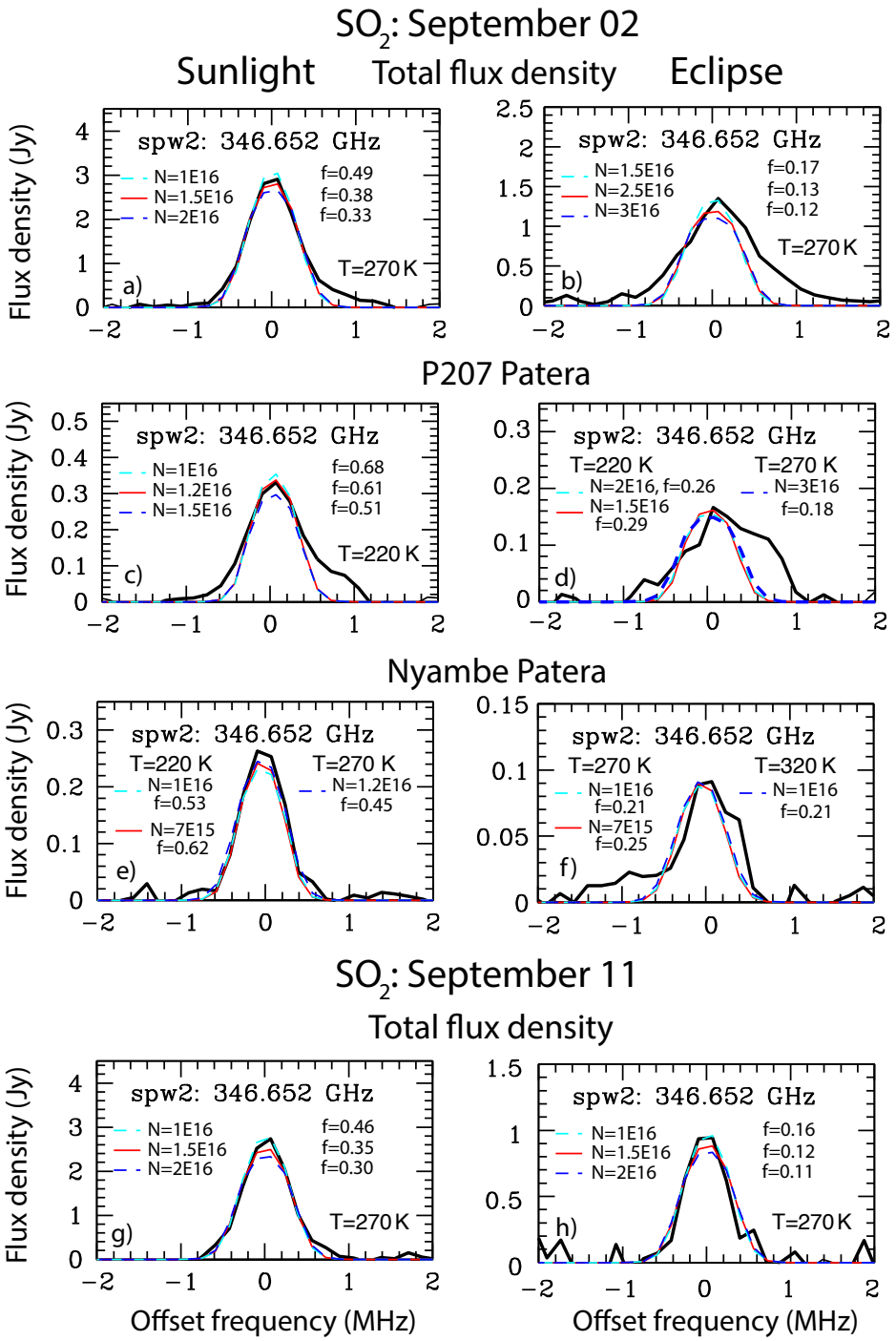


Figure 14. SO_2 line profiles (in black) with superposed various models. The red lines show the best fit models. All data and models are at 346.652 GHz (spw2). The temperature (T), column density (N), and fractional coverage (fr) are indicated for each model. Panels a–f) are for 2 September, g–h) for 11 September. a) Disk-integrated flux density for Io-in-sunlight. b) Disk-integrated flux density for Io-in-eclipse. c– d) Line profiles for P207 Patera in-sunlight and in-eclipse. e– f) Line profiles for Nyambe Patera in-sunlight and in-eclipse. g–h) Line profiles for the total flux density for 11 September in-sunlight and in-eclipse, respectively.

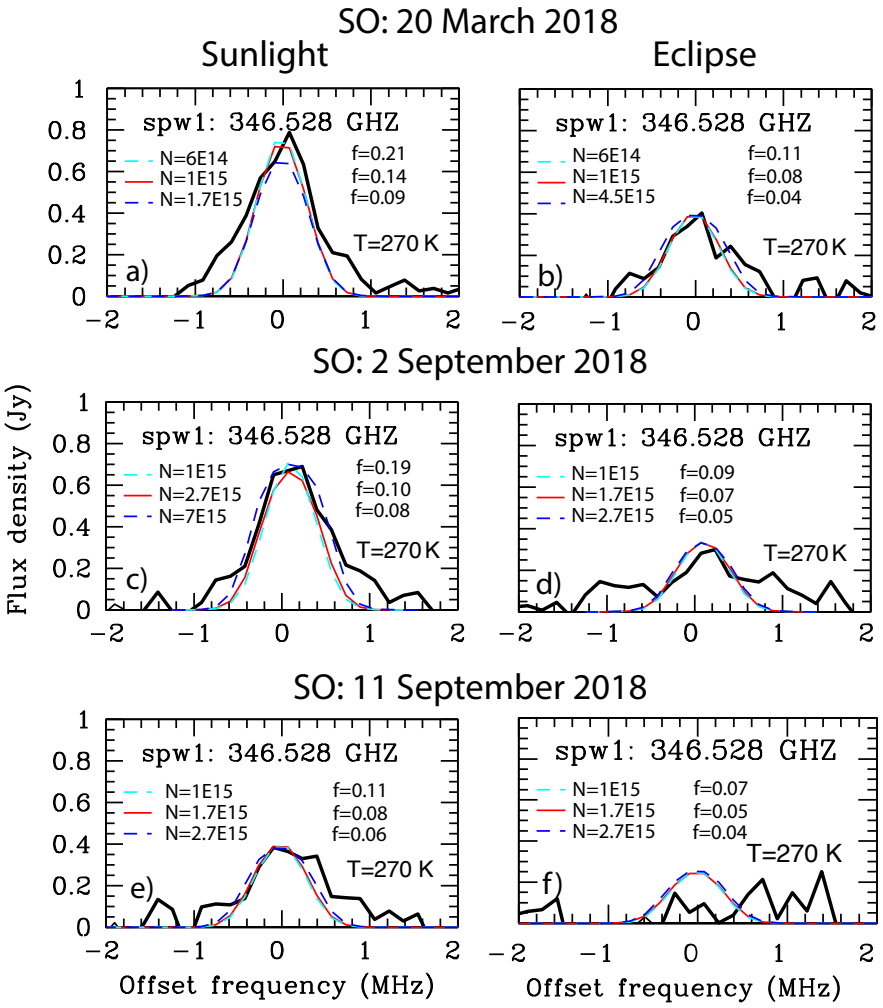


Figure 15. SO line profiles (in black) with superposed various hydrostatic models. The red lines show the best fits; all models shown are at 346.528 GHz (spw1). The temperature (T), column density (N), and fractional coverage (fr) are indicated for each model. On the left are SO profiles in-sunlight; on the right in-eclipse. The dates are indicated above each row. Note the shape of the profiles, and the variations in intensity.